Journal of Vibration Engineering & Technologies (2024) 12:1957–1977
https://doi.org/10.1007/s42417-023-00956-y

ORIGINAL PAPER

Analysis of Second-Order Thrust Bearing Coefficients Considering Misalignment Effect

Elsayed K. Elsayed[1] · Hussein Sayed[1,4] · T. A. El-Sayed[1,2,3]

Received: 30 October 2022 / Revised: 30 October 2022 / Accepted: 21 March 2023 / Published online: 28 April 2023

Abstract

Purpose Thrust bearings play a critical role in high-speed rotating machinery, such as turbines, pumps, compressors, and turbogenerators, by transferring axial loads between the collar and the bearing pads. The lubricating fluid prevents contact, friction, and wear between solid parts and acts as a cooling medium. The purpose of this study is to evaluate the first- and second-order bearing coefficients of an inclined pad hydrodynamic thrust bearing, which have not been previously investigated, to improve the accuracy of modeling thrust bearings.

Methods In the analysis of thrust bearing systems, the lubricating fluid film is modeled as a massless spring-damper system. The finite perturbation method for the governing Reynolds equation is used to calculate the dynamic coefficients of the thrust bearing. This is done using the finite difference method (FDM) in polar coordinates.

Results This study investigates the influence of misalignment, rotating speed, and mesh size on the bearing coefficients of the thrust bearing. The results show that misalignment angle and film thickness have a clear effect on the dynamic coefficients, while changing the rotational speed has no effect on the damping coefficients. The study also investigates the axial force and moments and dynamic coefficients of an inclined pad thrust bearing.

Conclusion This study concludes that evaluating the first- and second-order bearing coefficients of the thrust bearing using the finite perturbation method can improve the accuracy of modeling thrust bearings. The study also highlights the significant influence of misalignment and film thickness on the dynamic coefficients of the thrust bearing. The results presented in this study provide valuable data that can be used as input for rotor dynamics analyses in high-speed rotating machinery.

Keywords Thrust bearing · Reynolds equation · Finite difference method · Non-linear dynamic coefficients

✉ T. A. El-Sayed
tamer.elsayed@abdn.ac.uk

Elsayed K. Elsayed
khodrye@m-eng.helwan.edu.eg

Hussein Sayed
husseinsayed2008@m-eng.helwan.edu.eg

[1] Department of Mechanical Design, Faculty of Engineering, Mataria, Helwan University, Helmeiat-Elzaton, P. O. Box 11718, Cairo, Egypt

[2] Centre for Applied Dynamics Research, School of Engineering, University of Aberdeen, Aberdeen AB24 3UE, UK

[3] School of Engineering, University of Hertfordshire Hosted by Global Academic Foundation, Cairo, Egypt

[4] High Institute for Engineering and Technology Al-Obour, Km 21 Cairo-Belbeis Road, Obour City, Egypt

List of Symbols

$C_{\eta\zeta}$	1st order damping coefficients, $\eta, \zeta = z, \theta_x, \theta_y, \dot{z}, \dot{\theta}_x, \dot{\theta}_y$
$C_{\eta\zeta\gamma}$	2nd order damping coefficients $\eta, \zeta, \gamma = z, \theta_x, \theta_y, \dot{z}, \dot{\theta}_x, \dot{\theta}_y$
F_z	Bearing force in axial direction (N)
h	Fluid film thickness (m)
h_1	Minimum fluid film thickness (m)
h_s	Fluid film thickness at the inclined part (m)
h_{max}	Maximum fluid film thickness (m), $h_s = h_{max} - h_1$
$K_{\zeta\eta}$	First-order stiffness coefficients $\zeta, \eta = z, \theta_x, \theta_y$
$K_{\zeta\eta\gamma}$	Second-order stiffness coefficients $\zeta, \eta, \gamma = z, \theta_x, \theta_y$
M_x, M_y	Bearing moments in x and y directions (N.m)
n	Rotational speed (rpm)
p	Fluid film pressure (N/m^2)
r	Radial coordinate
r_i	Inner radius (m)
r_o	Outer radius (m)

t	Time (s)
v_θ	Mean journal speed (m/s), $((r_i + r_o)/2)\omega$
x, y, z	Cartesian coordinates
Δz	Axial displacement (m)
$\Delta \dot{z}$	Axial velocity (m/s)
μ	Lubricant viscosity (N.s/m^2)
ω	Angular velocity (rad/s)
θ	Circumferential coordinate
θ_{pad}	Thrust pad extend angle
$\theta x_0, \theta y_0$	Misalignment angles in x and y directions
$\Delta\theta_x, \Delta\theta_y$	Angular displacements around x and y directions
$\Delta\dot{\theta}_x, \Delta\dot{\theta}_y$	Angular velocities around x- and y-directions

Subscripts

0	Non-linear

Superscripts

f	First order
s	Second order

Introduction

Hydrodynamic thrust bearings are a machine elements that are used in rotating machinery to transfer thrust loads from a shaft to the bearing pads and used also to reduce wear and friction between the rotating "collar" and fixed "bearing pads" parts of the system [1]. As a lubricant of the thrust bearing, it provides stiffness and damping effect and prevents solid contact between stationary and rotating parts. Due to the importance of bearing stiffness and damping coefficients in the dynamic analysis of rotor-bearing system, many researchers have proposed several methods to calculate the dynamic coefficients of a hydrodynamic bearing.

The pressure distribution in hydrodynamic bearings is governed by the Reynolds equation which is derived from the continuity and Navier–Stokes equations [2]. Pinkus and Lynn [3] was the first who solve Reynolds equation numerically using the finite difference method (FDM) for the thrust bearing. Najar and Harmain [4] solved the Reynolds equation for sector shaped pad thrust bearing using FDM with several grid sizes. The pressure was evaluated at various locations after performing a through grid refinement. Koç [5] described a numerical method for solving Reynolds equation with aspect to thrust bearing using FDM. A theoretical model was developed to calculate the pressure distribution and load-carrying capacity for thrust bearing. Heshmat and Pinkus [6] introduced an analysis and computer solution for the tapered land thrust bearing considering misalignment for the thrust faces. The analysis includes the thermal effect and cavitation boundary conditions for different geometries. Someya and Fukuda [7] used two different methods to solve the Reynolds equation which are the non-linear method and linear method. The variation of the oil-film thickness and pressure for a hydrodynamic thrust bearing under periodic load was analyzed then verified experimentally. Vieira et al. [8] used a finite volume method to solve the Reynolds equation to find the pressure distribution and the load-carrying capacity in the polar coordinates. The equivalent direct axial stiffness and damping coefficients calculated from the pressure distribution and total load capacity. Vieira et al. [9] used FDM numerically to investigate the pressure distribution and load-carrying capacity of thrust bearing with different geometries. The effect of different operating parameters, such as oil viscosity, rotating speed, sector radii, and film thickness on pressure distribution and load capacity, were investigated. Ettles [10] introduced a computer program to simulate and analysis sector pad-shaped tilting thrust bearing. The program can solve the coupled elasticity, Reynolds, and energy equations. Using this program, the effect of different operating conditions on bearing performance can be investigated. Zhang et al. [11] carried out a simulation design and optimization for the thrust bearing capacity. The Reynolds equation for water-lubricated thrust bearing was solved to calculate the pressure distribution and load-carrying capacity. The theoretical results verified with the results obtained from the experimental work. Najar and Harmain [12] developed a finite difference-based numerical model to simulate the Reynolds equation. A new cooling circuit configuration considered, and it is observed that a significant amount of heat is removed from the cooling medium.

Kim, et al. [13] evaluated the pressure, load, stiffness, and damping of fluid dynamic bearings from generalized Reynolds equation and its perturbed equations after transferring these to finite-element equations. The proposed method was verified by comparing the results of coupled journal and conical bearing with the simulated method. Liming et al. [14] introduced a review about large tilting pad thrust bearing used in hydropower units. The review included the transient and dynamic characteristics, thermal–elastic deformation, and the different methods for bearing performance prediction. Jang and Lee [15] numerically calculated the first-order stiffness and damping coefficients of coupled journal and thrust bearing from Reynolds equation and its perturbed equations using finite-element method. X. Lin et al. [16, 17] proposed a lubricant model to investigate the static and dynamic characteristics of the spiral groove (SGTB) water-lubricated thrust bearing at high-speed. The proposed model considered the centrifugal and cavitating effects in calculations. Lin et al. [18] studied the effect of interface effect and cavitation bubble on the dynamic characteristics of water-lubricated spiral groove thrust bearing. The perturbed Reynolds equation was solved to calculate the stiffness and damping coefficients of thrust bearing. The theoretical results were verified with a developed experiment. The results showed

that the dynamic coefficients of spiral groove thrust bearing are highly affected by cavitation and turbulent effect. Jialei and Liang [19] calculated the stiffness and damping coefficients of hydrostatic bearing using an improved method based on the mathematical perturbation technique. The calculated dynamic coefficients from the improved method and the convectional method were compared to validate the effectiveness of the improved method. Peixoto et.al. [20–23] estimated the first-order stiffness and damping coefficients of the thrust bearing by small perturbation around the equilibrium position using finite-element method and compared the calculated coefficients with the experimental results. Yadav et al. [24] computed the stiffness and damping of aerostatic thrust bearing with different recess geometries using the finite-element method. The influence of tilt angle on the aerostatic thrust bearing performance was also analyzed. Lin and Hung [25] presented a dynamic analysis of a wide slider with exponential film profile considering the squeeze action. The dynamic coefficients were evaluated from the perturbed Reynolds equation and were compared with the inclined plane profile.

Koutsoumpas, et al. [26] developed a CFD-based thermo-hydrodynamic (THD) numerical model to estimate the stiffness and damping coefficients of the thrust bearing at different operating conditions. Srikanth et al. [27] described a finite difference technique to solve Reynolds and temperature distribution for thrust bearing considering viscosity variation. The angular stiffness coefficient, pad deformation, and torque were calculated from a coupled finite-element method using ANSYS. Iordanoff et al. [28, 29] used the small perturbation method to solve the Reynolds equation to estimate the stiffness and damping coefficients considering axial and misalignment movements. Storteig and White [30] used one-dimensional finite-element technique to solve Reynolds equation and the pressure assumed to be in the radial direction and the thermal effect included. Then, the dynamic coefficients calculated for fixed pad thrust bearing at different geometries. Gad [31, 32] analyzed the stiffness and damping coefficients, power losses, and load capacity of the gas film thrust bearings at small angular misalignments. A small perturbation method was used to evaluate the dynamic coefficients and study the effect of static and dynamic angular misalignments on the performance of gas-lubricated foil thrust bearing. Shi, et al. [33] solved the coupled perturbed Reynolds equation for a 3-DOF aerostatic thrust bearing with orifice restrictor. The effect of film thickness, rotating speed, perturbation factor, and tilt angle on the thrust bearing characteristics are evaluated. L. San Andre's [34] evaluated the effect of misalignment on the dynamic performance of a hybrid thrust bearing. Zero- and first-order equations were obtained by introducing a small axial and angular motions to the perturbed analysis. Sun et al. [35] established a 5-DOF model of the rotor and 3-DOF model for rubber supported water-lubricated thrust bearing. A mixed thermoelastohydrodynamic (TEHD) model used to study the dynamic effect of the thrust bearing on the system response under external disturbing moments and the results verified experimentally. Nitzschke et al. [36] studied the floating-ring thrust bearing and its effect on the transient rotor-dynamic simulation by solving the Reynolds equation. The coupling effect between the different fluid films is simulated and the difference between coupled and uncoupled solution is discussed.

Kim Jang and Kim [37] presented a 5-DOF model for a general rotor-bearing system to calculate the stiffness and damping coefficients in a hydrodynamic bearings. A small amplitude motion of a bearing center is assumed to obtain the perturbed equations from Reynolds equation. Then, the dynamic coefficients are obtained for journal and thrust bearing due to eccentricity and misalignment. Jintanawan et al. [38] investigated the thrust bearing axial stiffness and damping coefficients, and studied the effect of these coefficients on the axial vibration of disk-spindle system in hard disk drives. Temis and Lazarev [39] developed a model to calculate the stiffness and damping coefficients of thrust bearing considering axial and angular motion. The obtained results were compared with the results from STAR-CD software and the theoretical and experimental results in the previous literature. Srikanth et al. [40] used a finite difference method to solve the Reynolds equation to find the pressure distribution and load-carrying capacity for thrust bearing. The dynamic stiffness and damping obtained by varying the film thickness and introducing a velocity to the runner.

The radial journal bearing literature shows many attempts to use second-order and higher order bearing coefficients; see, for example, [41–47]. The authors of these articles showed that using higher order bearing coefficients gives better approximation to the non-linear bearing forces and to the stability analysis. Meanwhile, the literature for thrust bearing shows a significant gap in evaluating higher order bearing coefficient for thrust bearing. This motivates the authors to fill this gap and investigate the significance of evaluating the second-order bearing coefficients.

In this article, the finite perturbation method used in reference [37] is extended to find the second-order dynamic coefficients for inclined pad thrust bearing considering a 3 degrees of freedom. The finite difference method is used to find the pressure distribution and load-carrying capacity for thrust bearing. The first- and second-order dynamic coefficients are obtained by introducing a small perturbation displacements and velocities of shaft motion and the effects of the misalignments on the dynamic coefficients are discussed. This method is appropriate for different types of thrust bearings and provide a prediction of fluid film forces

and moments in non-linear dynamic analysis of fluid film rotor-bearing system.

Theoretical Analysis

In this section, the pressure distribution of the thrust bearing is calculated using finite difference method. The calculated pressure is used to calculate load-carrying capacity, stiffness, and damping coefficients of the hydrodynamic thrust bearing. The assumptions for Reynolds equation are the fluid film is laminar, Newtonian, isothermal, and incompressible. In addition, it is assumed that there is no cavitation, and the body inertia forces are negligible. The geometry of the bearing studied in the simulation is inclined pad thrust bearing, as shown in Fig. 1. The Reynolds equation governing oil-film pressure distribution has the following form:

$$\frac{\partial}{r\partial r}\left(\frac{rh^3}{12\mu}\frac{\partial p}{\partial r}\right)+\frac{1}{r}\frac{\partial}{\partial\theta}\left(\frac{h^3}{12\mu}\frac{\partial p}{r\partial\theta}\right)=\frac{v_\theta}{r}\frac{\partial h}{\partial\theta}+\frac{\partial h}{\partial t}, \tag{1}$$

where μ is the lubricant viscosity, and r and θ are the radial and circumferential coordinates, respectively. p and h are the oil-film pressure and thickness, respectively. v_θ is the mean speed of journal, and t is the time. The fluid film thickness of the bearing in the static equilibrium state can be determined as follows:

$$h_{static}=\begin{cases} h_1+h_s\left(1-\frac{\theta}{\theta_{pad}}\right) & \text{(Inclined pad)} \\ h_{max} & \text{(groove)}, \end{cases} \tag{2}$$

where h_1 is the minimum film thickness, h_s is the tapper land height, and θ_{pad} is the pad extend angle. The finite perturbation method is used to calculate the dynamic coefficients of the fluid film bearing. Accordingly, the steady-state position of the runner is perturbed by small translational displacement (Δz), small rotational displacements ($\Delta\theta_x$ and $\Delta\theta_y$), small translational velocity ($\Delta\dot{z}$), and small rotational velocities ($\Delta\dot{\theta}_x$ and $\Delta\dot{\theta}_y$). From Fig. 2, the film thickness between the bearing and the collar can be expressed as follows:

$$h=h_0-r\Delta\theta_x\sin\theta+r\Delta\theta_y\cos\theta+\Delta z, \tag{3}$$

where h_0 is the film thickness at the equilibrium position which has the following form:

$$h_0=h_{static}-r\theta_{x_0}\sin\theta+r\theta_{y_0}\cos\theta+z_{min}. \tag{4}$$

The thrust plate position can be obtained from the clearance and misalignment angles. In differentiation of the film thickness with respect to time, Eq. 3 can be written in the following form:

$$\frac{\partial h}{\partial t}=-r\Delta\dot{\theta}x\sin\theta+r\Delta\dot{\theta}y\cos\theta+\Delta\dot{z}. \tag{5}$$

The small perturbation of the fluid film will produce perturbation in the fluid film pressure. The perturbed pressure distribution can be obtained by the following expression:

$$p=p_0+\sum_{\zeta}p_\zeta\Delta\zeta+\sum_{\dot{\zeta}}p_{\dot{\zeta}}\Delta\dot{\zeta}, \tag{6}$$

where $\zeta=z,\ \theta_x,\ \theta_y$ and $\dot{\zeta}=\dot{z},\ \dot{\theta}_x,\ \dot{\theta}_y$.

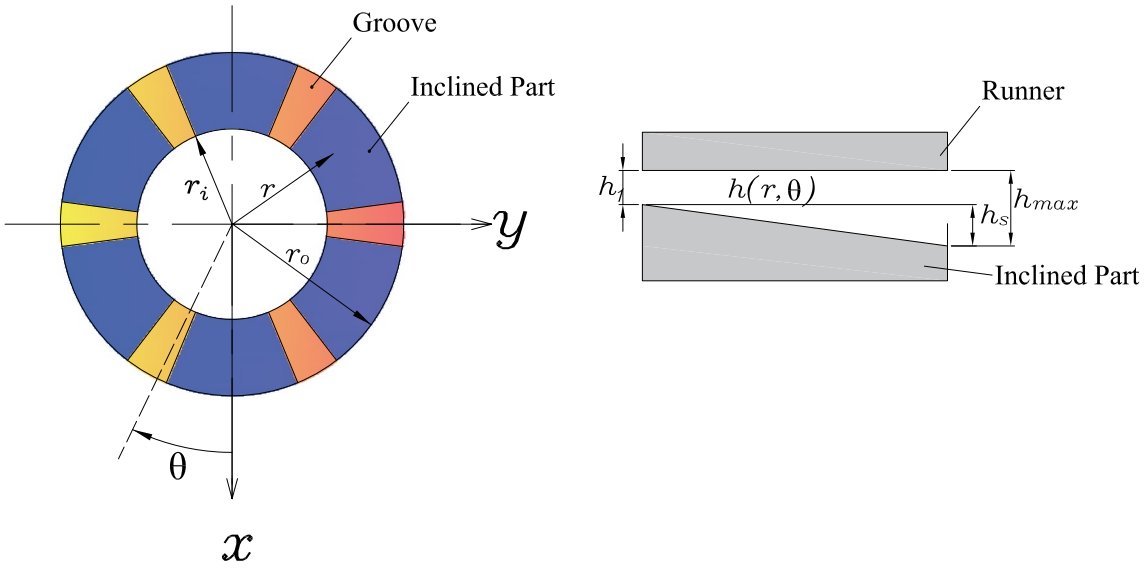

Fig. 1 Hydrodynamic thrust bearing geometric structure. **a** Thrust pad which consist of 6 pads each of 45° angular extend and 6 grooves each of 15° angular extend. **b** Pad surface profile and film thickness illustration

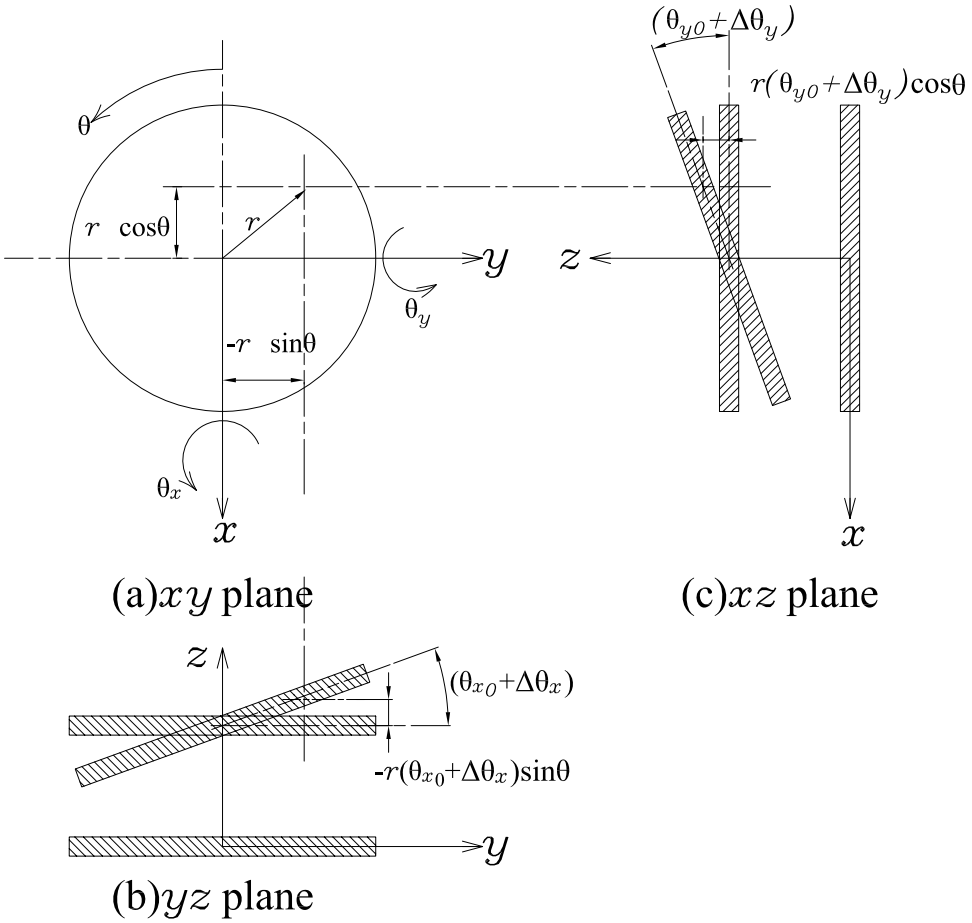

Fig. 2 Hydrodynamic thrust bearing with tilt angles θ_{x_0} and θ_{y_0}: **a** *xy* plane, **b** *yz* plane, and **c** *xz* plane [37]

Reynolds equation [Eq. 1] resolved by substituting Eqs. (3), (5, 6) into Eq. (1). Six perturbed equations are obtained to calculate the first-order damping and stiffness coefficients of the thrust bearing which can be obtained by the following two equations:

$$\begin{aligned}&\left(\frac{3h^2h_\zeta}{12\mu r}+\frac{6hh_\zeta h_r}{12\mu}+\frac{3h^2h_{r\zeta}}{12\mu}\right)p_r+\left(\frac{h^3}{12\mu r}+\frac{3h^2h_r}{12\mu}\right)\\&p_{r\zeta}+\left(\frac{3h^2h_\zeta}{12\mu}\right)p_{rr}+\left(\frac{h^3}{12\mu}\right)p_{rr\zeta}+\\&\left(\frac{6hh_\zeta h_\theta}{12\mu r^2}+\frac{3h^2h_{\theta\zeta}}{12\mu r^2}\right)p_\theta+\left(\frac{3h^2h_\theta}{12\mu r^2}\right)p_{\theta\zeta}+\left(\frac{3h^2h_\zeta}{12\mu r^2}\right)\\&p_{\theta\theta}+\left(\frac{h^3}{12\mu r^2}\right)p_{\theta\theta\zeta}=\frac{v_\theta}{r}h_{\theta\zeta},\end{aligned}\tag{7}$$

and

$$\begin{aligned}&\left(\frac{h^3}{12\mu r}+\frac{3h^2h_r}{12\mu}\right)p_{r\dot\zeta}+\left(\frac{h^3}{12\mu}\right)p_{rr\dot\zeta}+\left(\frac{3h^2h_\theta}{12\mu r^2}\right)\\&p_{\theta\dot\zeta}+\left(\frac{h^3}{12\mu r^2}\right)p_{\theta\theta\dot\zeta}=h_{\dot\zeta},\end{aligned}\tag{8}$$

where $\zeta = z,\ \theta_x,\ \theta_y$ and $\dot\zeta = \dot z,\ \dot\theta_x,\ \dot\theta_y$,

$$p_r=\frac{\partial p}{\partial r},\ p_{rr}=\frac{\partial}{\partial r}\left(\frac{\partial p}{\partial r}\right),$$

$$p_\theta=\frac{\partial p}{\partial\theta},p_{\theta\theta}=\frac{\partial}{\partial\theta}\left(\frac{\partial p}{\partial\theta}\right),$$

$$h_r=\frac{\partial h}{\partial r}=-\theta_{x_0}\sin\theta+\theta_{y_0}\cos\theta,$$

$$h_\theta=\frac{\partial h}{\partial\theta}=\begin{cases}-\frac{h_s}{\theta_{pad}}-r\theta_{x_0}\cos\theta-r\theta_{y_0}\sin\theta & \text{(Inclined pad)},\\ -r\theta_{x_0}\cos\theta-r\theta_{y_0}\sin\theta & \text{(Groove)}.\end{cases}$$

Calculation of the Load-Carrying Capacity and First-Order Dynamic Coefficients

The solution of the seven perturbed pressure Eqs. (1, 7, 8) is obtained using the finite difference method to determine the bearing load-carrying capacity, reaction forces, and moments as follows: where p_0 is calculated using Eq. (1) at $\frac{\partial h}{\partial t} = 0$:

$$\boldsymbol{F}_0 = \begin{Bmatrix} F_{z_0} \\ M_{x_0} \\ M_{y_0} \end{Bmatrix} = \iint\limits_{r,\theta} \begin{Bmatrix} -p_0 \\ p_0 r \sin\theta \\ -p_0 r \cos\theta \end{Bmatrix} r \, \mathrm{d}r \, \mathrm{d}\theta, \tag{9}$$

$$\begin{Bmatrix} F_z^f \\ M_x^f \\ M_y^f \end{Bmatrix} = \iint\limits_{r,\theta} \left\{ p_0 + \sum_{\zeta} p_\zeta \Delta\zeta + \sum_{\zeta} p_{\dot{\zeta}} \Delta\dot{\zeta} \right\} \begin{Bmatrix} -1 \\ r\sin\theta \\ -r\cos\theta \end{Bmatrix} r \, \mathrm{d}r \, \mathrm{d}\theta = \boldsymbol{F}_0 + \boldsymbol{K}_{\eta\zeta} \begin{Bmatrix} \Delta z \\ \Delta\theta_x \\ \Delta\theta_y \end{Bmatrix} + \boldsymbol{C}_{\eta\zeta} \begin{Bmatrix} \Delta\dot{z} \\ \Delta\dot{\theta}_x \\ \Delta\dot{\theta}_y \end{Bmatrix}, \tag{10}$$

where $\boldsymbol{F}_0$ is the load-carrying capacity, $\boldsymbol{K}_{\eta\zeta}$ is the first-order stiffness matrix, and $\boldsymbol{C}_{\eta\zeta}$ is the first-order damping matrix which can be expressed as follows:

$$\boldsymbol{K}_{\eta\zeta} = \begin{bmatrix} K_{zz} & K_{z\theta_x} & K_{z\theta_y} \\ K_{\theta_x z} & K_{\theta_x\theta_x} & K_{\theta_x\theta_y} \\ K_{\theta_y z} & K_{\theta_y\theta_x} & K_{\theta_y\theta_y} \end{bmatrix} = \iint\limits_{r,\theta} \begin{Bmatrix} -1 \\ r\sin\theta \\ -r\cos\theta \end{Bmatrix} \{ p_z \; p_{\theta x} \; p_{\theta y} \} r \, \mathrm{d}r \, \mathrm{d}\theta, \tag{11}$$

$$\boldsymbol{C}_{\eta\zeta} = \begin{bmatrix} C_{zz} & C_{z\theta_x} & C_{z\theta_y} \\ C_{\theta_x z} & C_{\theta_x\theta_x} & C_{\theta_x\theta_y} \\ C_{\theta_y z} & C_{\theta_y\theta_x} & C_{\theta_y\theta_y} \end{bmatrix} = \iint\limits_{r,\theta} \begin{Bmatrix} -1 \\ r\sin\theta \\ -r\cos\theta \end{Bmatrix} \{ p_{\dot{z}} \; p_{\dot{\theta}x} \; p_{\dot{\theta}y} \} r \, \mathrm{d}r \, \mathrm{d}\theta, \tag{12}$$

for which $K_{zz} = \frac{\partial F_z}{\partial z}$, $K_{z\theta_x} = \frac{\partial F_z}{\partial \theta_x}$, $C_{zz} = \frac{\partial F_z}{\partial \dot{z}}$, $C_{z\theta_x} = \frac{\partial F_z}{\partial \dot{\theta}_x}$, and so on.

Calculation of Second-Order Non-linear Dynamic Coefficients

The six perturbed pressure equations obtained from Eqs. (7, 8) in the first-order dynamic analysis are differentiated with respect to $(z, \theta_x, \theta_y, \dot{z}, \dot{\theta}_x, \dot{\theta}_y)$ for every equation individually to get the second-order perturbed equations as follows:

$$\begin{aligned}
&\left(\frac{6hh_\zeta h_\gamma}{12\mu r} + \frac{6h_\zeta h_\gamma h_r + 6hh_\zeta h_{r\gamma} + 6hh_\gamma h_{r\zeta}}{12\mu} \right) \\
&p_r + \left(\frac{3h^2 h_\zeta}{12\mu r} + \frac{6hh_\zeta h_r + 3h^2 h_{r\zeta}}{12\mu} \right) p_{r\gamma} \\
&+ \left(\frac{3h^2 h_\gamma}{12\mu r} + \frac{6hh_\gamma h_r + 3h^2 h_{r\gamma}}{12\mu} \right) \\
&p_{r\zeta} + \left(\frac{h^3}{12\mu r} + \frac{3h^2 h_r}{12\mu} \right) p_{r\zeta\gamma} + \left(\frac{6hh_\zeta h_\gamma}{12\mu} \right) p_{rr} \\
&+ \left(\frac{3h^2 h_\zeta}{12\mu} \right) p_{rr\gamma} + \left(\frac{3h^2 h_\gamma}{12\mu} \right) p_{rr\zeta} + \left(\frac{h^3}{12\mu} \right) p_{rr\zeta\gamma} \\
&+ \left(\frac{6h_\zeta h_\gamma h_\theta + 6hh_\zeta h_{\theta\gamma} + 6hh_\gamma h_{\theta\zeta}}{12\mu r^2} \right) \\
&p_\theta + \left(\frac{6hh_\zeta h_\theta + 3h^2 h_{\theta\zeta}}{12\mu r^2} \right) p_{\theta\gamma} \\
&+ \left(\frac{6hh_\gamma h_\theta + 3h^2 h_{\theta\gamma}}{12\mu r^2} \right) p_{\theta\zeta} + \left(\frac{3h^2 h_\theta}{12\mu r^2} \right) p_{\theta\zeta\gamma} + \left(\frac{6hh_\zeta h_\gamma}{12\mu r^2} \right) p_{\theta\theta} \\
&+ \left(\frac{3h^2 h_\zeta}{12\mu r^2} \right) p_{\theta\theta\gamma} + \left(\frac{3h^2 h_\gamma}{12\mu r^2} \right) p_{\theta\theta\zeta} + \left(\frac{h^3}{12\mu r^2} \right) p_{\theta\theta\zeta\gamma} = 0,
\end{aligned} \tag{13}$$

and

$$\begin{aligned}
&\left(\frac{3h^2 h_\zeta}{12\mu r} + \frac{6hh_\zeta h_r}{12\mu} + \frac{3h^2 h_{r\zeta}}{12\mu} \right) \\
&p_{r\dot{\gamma}} + \left(\frac{h^3}{12\mu r} + \frac{3h^2 h_r}{12\mu} \right) p_{r\zeta\dot{\gamma}} + \left(\frac{3h^2 h_\zeta}{12\mu} \right) \\
&p_{rr\dot{\gamma}} + \left(\frac{h^3}{12\mu} \right) p_{rr\zeta\dot{\gamma}} \\
&+ \left(\frac{6hh_\zeta h_\theta}{12\mu r^2} + \frac{3h^2 h_{\theta\zeta}}{12\mu r^2} \right) p_{\theta\dot{\gamma}} + \left(\frac{3h^2 h_\theta}{12\mu r^2} \right) p_{\theta\zeta\dot{\gamma}} + \left(\frac{3h^2 h_\zeta}{12\mu r^2} \right) \\
&p_{\theta\theta\dot{\gamma}} + \left(\frac{h^3}{12\mu r^2} \right) p_{\theta\theta\zeta\dot{\gamma}} = 0,
\end{aligned} \tag{14}$$

where

$$\zeta, \gamma = z, \; \theta_x, \; \theta_y \quad \& \dot{\gamma} = \dot{z}, \; \dot{\theta}_x, \; \dot{\theta}_y \qquad h_{\zeta\gamma} = 0.$$

Previous equations [Eqs. (13, 14)] are solved using finite difference method to calculate the second-order dynamic coefficients as follows:

$$
\begin{Bmatrix} F_z^s \\ M_x^s \\ M_y^s \end{Bmatrix}
= \iint_{r,\theta} \left\{ p_o + \sum_{\zeta} p_{\zeta} \Delta\zeta + \sum_{\zeta} p_{\dot{\zeta}} \Delta_{\dot{\zeta}} + \frac{1}{2} \sum_{\zeta\gamma} p_{\zeta\gamma} \Delta\zeta \Delta\gamma + \sum_{\zeta\gamma} p_{\zeta\dot{\gamma}} \Delta\zeta \Delta\dot{\gamma} \right\}
\times \begin{Bmatrix} -1 \\ r\sin\theta \\ -r\cos\theta \end{Bmatrix} r \mathrm{d}r\mathrm{d}\theta
$$

$$
= \boldsymbol{F}_0 + \boldsymbol{K}_{\eta\zeta} \begin{Bmatrix} \Delta z \\ \Delta\theta_x \\ \Delta\theta_y \end{Bmatrix} + \boldsymbol{C}_{\eta\zeta} \begin{Bmatrix} \Delta\dot{z} \\ \Delta\dot{\theta}_x \\ \Delta\dot{\theta}_y \end{Bmatrix} + \boldsymbol{K}_{\eta\zeta\gamma} \begin{Bmatrix} 0.5\Delta z^2 \\ \Delta z\Delta\theta_x \\ \Delta z\Delta\theta_y \\ 0.5\Delta\theta_x{}^2 \\ \Delta\theta_x\Delta\theta_y \\ 0.5\Delta\theta_y{}^2 \end{Bmatrix}
$$

$$
+ \boldsymbol{C}_{\eta\zeta\gamma} \begin{Bmatrix} \Delta z\Delta\dot{z} \\ \Delta z\Delta\dot{\theta}_x \\ \Delta z\Delta\dot{\theta}_y \\ \Delta\theta_x\Delta\dot{z} \\ \Delta\theta_x\Delta\dot{\theta}_x \\ \Delta\theta_x\Delta\dot{\theta}_y \\ \Delta\theta_y\Delta\dot{z} \\ \Delta\theta_y\Delta\dot{\theta}_x \\ \Delta\theta_y\Delta\dot{\theta}_y \end{Bmatrix}, \tag{15}
$$

where $\zeta, \gamma = z,\ \theta_x$ and θ_y. $\boldsymbol{K}_{\eta\zeta\gamma}$ is the second-order stiffness matrix, and $\boldsymbol{C}_{\eta\zeta\gamma}$ is the second-order damping matrix which can be expressed as follows:

$$
\boldsymbol{K}_{\eta\zeta\gamma} = \begin{bmatrix} K_{zzz} & K_{zz\theta_x} & K_{zz\theta_y} & K_{z\theta_x\theta_x} & K_{z\theta_x\theta_y} & K_{z\theta_y\theta_y} \\ K_{\theta_x zz} & K_{\theta_x z\theta_x} & K_{\theta_x z\theta_y} & K_{\theta_x\theta_x\theta_x} & K_{\theta_x\theta_x\theta_y} & K_{\theta_x\theta_y\theta_y} \\ K_{\theta_y zz} & K_{\theta_y z\theta_x} & K_{\theta_y z\theta_y} & K_{\theta_y\theta_x\theta_x} & K_{\theta_y\theta_x\theta_y} & K_{\theta_y\theta_y\theta_y} \end{bmatrix}
$$

$$
= \iint_{r,\theta} \begin{Bmatrix} -1 \\ r\sin\theta \\ -r\cos\theta \end{Bmatrix} \begin{Bmatrix} p_{zz} & p_{z\theta_x} & p_{z\theta_y} & p_{\theta_x\theta_x} & p_{\theta_x\theta_y} & p_{\theta_y\theta_y} \end{Bmatrix} r \mathrm{d}r\mathrm{d}\theta, \tag{16}
$$

$$
\mathrm{C}_{\eta\zeta\gamma} = \begin{bmatrix} C_{zzz} & C_{zz\theta_x} & C_{zz\theta_y} & C_{z\theta_x z} & C_{z\theta_x\theta_x} & C_{z\theta_x\theta_y} & C_{z\theta_y z} & C_{z\theta_y\theta_x} & C_{z\theta_y\theta_y} \\ C_{\theta_x zz} & C_{\theta_x z\theta_x} & C_{\theta_x z\theta_y} & C_{\theta_x\theta_x z} & C_{\theta_x\theta_x\theta_x} & C_{\theta_x\theta_x\theta_y} & C_{\theta_x\theta_y z} & C_{\theta_x\theta_y\theta_x} & C_{\theta_x\theta_y\theta_y} \\ C_{\theta_y zz} & C_{\theta_y z\theta_x} & C_{\theta_y z\theta_y} & C_{\theta_y\theta_x z} & C_{\theta_y\theta_x\theta_x} & C_{\theta_y\theta_x\theta_y} & C_{\theta_y\theta_y z} & C_{\theta_y\theta_y\theta_x} & C_{\theta_y\theta_y\theta_y} \end{bmatrix}
$$

$$
= \iint_{r,\theta} \begin{Bmatrix} -1 \\ r\sin\theta \\ -r\cos\theta \end{Bmatrix} \begin{Bmatrix} p_{zz} & p_{z\dot{\theta}_x} & p_{z\dot{\theta}_y} & p_{\theta_x\dot{z}} & p_{\theta_x\dot{\theta}_x} & p_{\theta_x\dot{\theta}_y} & p_{\theta_y\dot{z}} & p_{\theta_y\dot{\theta}_x} & p_{\theta_y\dot{\theta}_y} \end{Bmatrix} r \mathrm{d}r\mathrm{d}\theta, \tag{17}
$$

for which $K_{zzz} = \frac{\partial F_z}{\partial z^2}, K_{zz\theta_x} = \frac{\partial F_z}{\partial z \partial \theta_x},\ C_{zzz} = \frac{\partial F_z}{\partial z \partial \dot{z}}, C_{zz\theta_x} = \frac{\partial F_z}{\partial z \partial \dot{\theta}_x}$, and so on.

Results and Discussion

In this section, a computer program is developed to study and analyze an inclined pad thrust bearing with six pads which its computational parameters are given in Table 1. In the present work, the Gauss–Seidel iterative numerical method has been used to solve the boundary value problem and the finite difference method is used to replace the partial derivatives in the pressure Eqs. (7, 8, 13 and 14) with suitable finite difference operators. A very efficient iterative solution approach is the so-called successive over-relaxation (SOR) method that is used to accelerate the solution convergence process. The first- and second-order dynamic coefficients of the thrust bearing are investigated with the consideration of shaft misalignment. The shaft is assumed to have a misaligned angle in θ_{x_0} direction. The infinitesimal perturbation method is used in the analysis.

As the shaft rotates, it drags the lubricating oil into the gap between the collar and the bearing pads and a hydrodynamic pressure is developed in the fluid film. The hydrodynamic pressure distribution for aligned thrust bearing is shown in Fig. 3. As it is clear from the figure, the pressure distribution is equal on all the bearing pads, as expected. Figure 4 shows the pressure distribution when the runner surface is allowed to tilt around x-axis. The flowchart of the numerical solution procedure is shown in Appendix B.

Bearing Force and Moment

The bearing force and moment are obtained for inclined pad thrust bearing using the perturbation analysis. The force and moment are calculated by applying a small, perturbed displacements and velocities to the equilibrium position for the three different methods [based on Reynolds equation ($F_{z\,Re}, M_{x\,Re}, M_{yRe}$), the first-order coefficients (F_{z1}, M_{x1}, M_{y1}) and the second-order coefficients (F_{z2}, M_{x2}, M_{y2})]. Three

Table 1 Thrust bearing computational parameters

Design parameter	Value
Viscosity, η	0.036 [N.s/m^2]
Minimum film thickness, h_1	75 e^{-6} [m]
Maximum film thickness, h_{max}	85 e^{-6} [m]
Taper depth, h_s	10 e^{-6} [m]
Rotational speed, n	7200 [rpm]
Pad angle, θ_{pad}	45°
Groove angle, θ_{groove}	15°
Inner radius, r_i	20 e^{-3} [m]
Outer radius, r_0	40 e^{-3} [m]

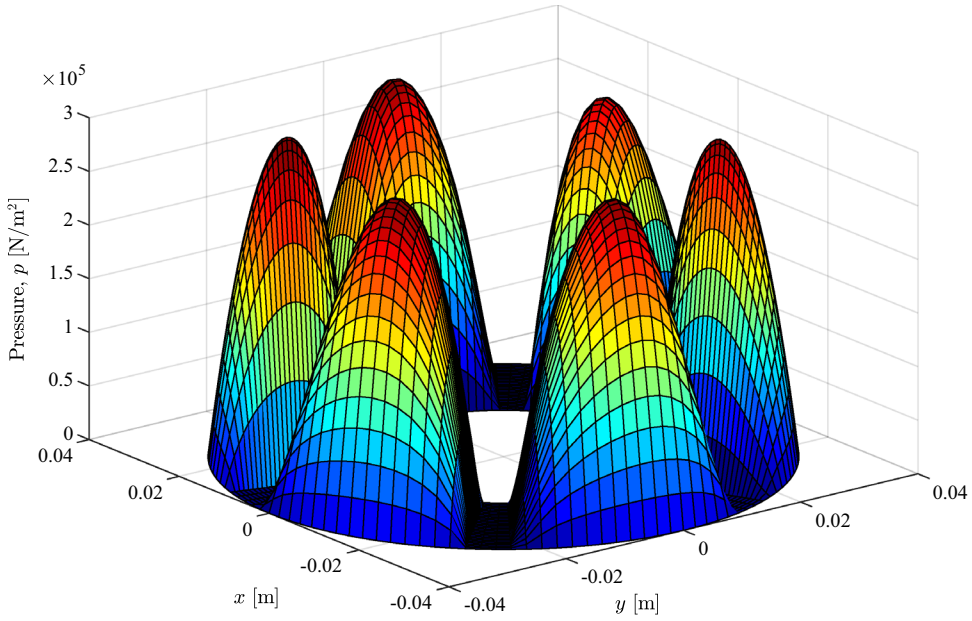

Fig. 3 Pressure distribution for aligned thrust bearing at $\theta_{x_0} = 0, n = 7200$ rpm, and $h_s = 10$ e−5 m

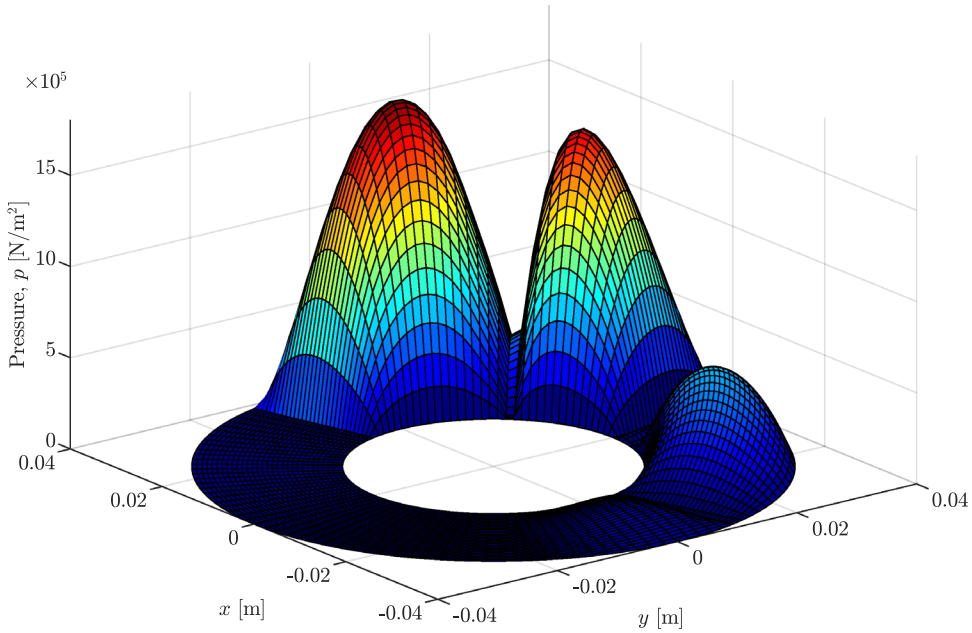

Fig. 4 Hydrodynamic pressure distribution for misaligned thrust bearing at $\theta_{x_0} = 0.96$e−3 radian, $n = 7200$ rpm, and $h_s = 10\ \mathrm{e}^{-6}$ m

Table 2 Perturbed values used in calculations

Case	Δz	$\Delta\theta_x$	$\Delta\theta_y$	$\Delta\dot{z}$	$\Delta\dot{\theta}_x$	$\Delta\dot{\theta}_y$
a	$1e^{-4} \times h_0$	$1e^{-6}$	$1e^{-6}$	$1e^{-4} \times \omega \times h_0$	$1e^{-6} \times \omega$	$1e^{-6} \times \omega$
b	$1e^{-3} \times h_0$	$1e^{-5}$	$1e^{-5}$	$1e^{-3} \times \omega \times h_0$	$1e^{-5} \times \omega$	$1e^{-5} \times \omega$
c	$1e^{-2} \times h_0$	$1e^{-4}$	$1e^{-4}$	$1e^{-2} \times \omega \times h_0$	$1e^{-4} \times \omega$	$1e^{-4} \times \omega$

different perturbation values are used to calculate the bearing forces and moments, as shown in Table 2.

Figure 5 shows the variation of the bearing force and moment with misalignment angle θ_{x_0}. At small values of perturbation, the values of forces and moments calculated by the three different methods are almost the same as each other, as shown in Fig. 5a, b. The higher the perturbation value, the clearer the difference between the values

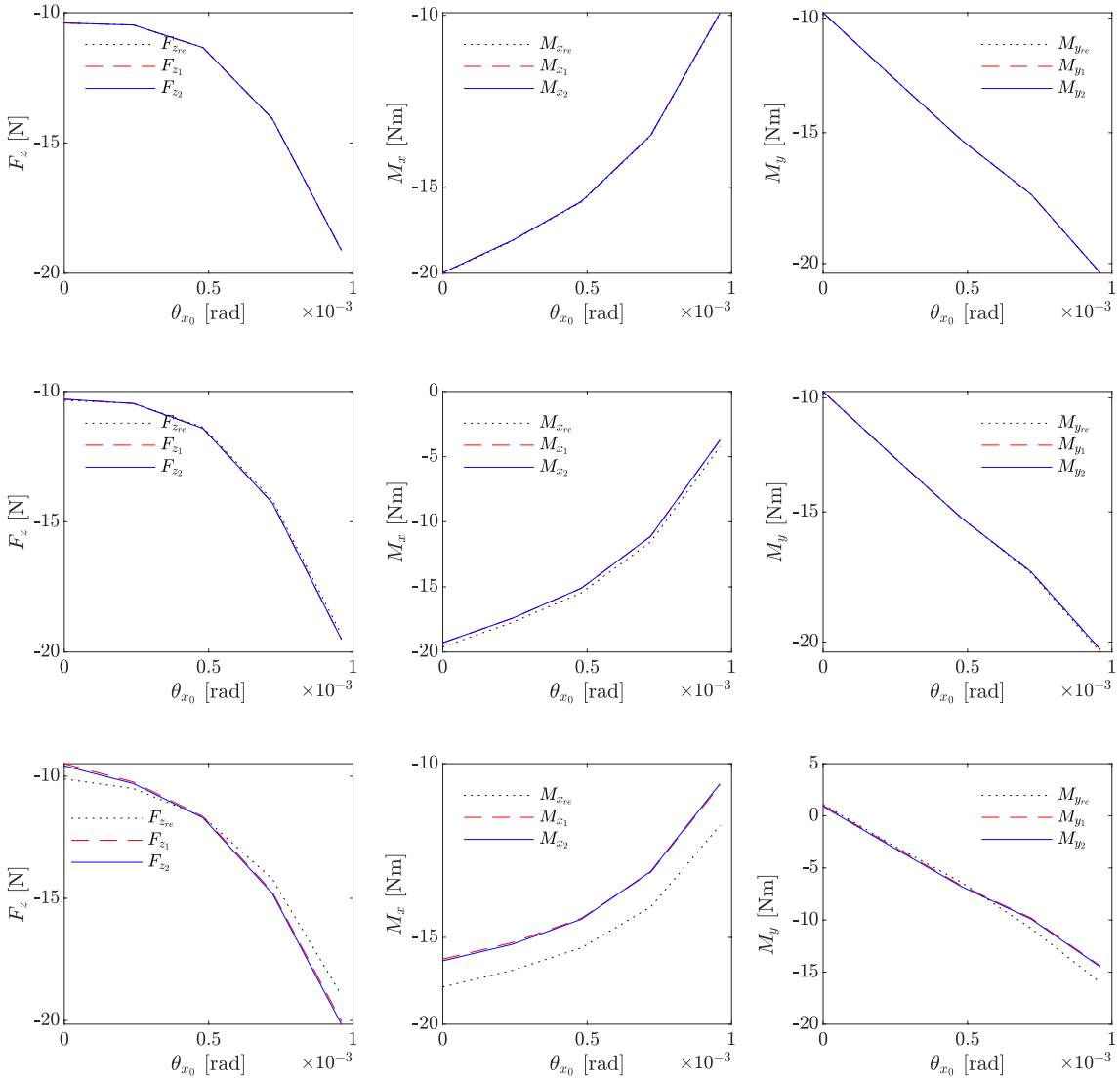

Fig. 5 Thrust bearing axial force F_z (first column), moment about x axis M_x (second column), and moment about y axis M_y (last column) versus the misalignment angle θ_{x_0}. Three perturbations from the equilibrium position are used as indicated in Table2, case (a) is presented in the first row, case (b) is presented in the second raw, and case (c) is displayed in the third row. The force and moments are calculated using three methods, (1) integration of Reynolds equation (dotted lines), (2) first-order coefficients (dashed lines), and (3) second-order coefficients (solid lines)

of forces and moments calculated using the three different methods, as shown in Fig. 5c.

Effect of Mesh Size and Misalignment (θ_{x_0})

In this section, the effect of mesh size on the dynamic coefficients of inclined pad thrust bearing is investigated. The first- and second-order dynamic coefficients are plotted in Figs. 6 and 7. The misalignment angle θ_{x_0} assumed to change from 0 to 0.00096 radian at a rotational speed, n of 7200 rpm. There are nine stiffness coefficients and nine damping coefficients for the first-order analysis, as shown in Fig. 6a, b. The second-order coefficients are 18 stiffness coefficients in addition to 27 damping coefficients. From the 27 damping coefficients, only nine second-order damping coefficients have values and the rest equal zero. Four mesh sizes are used to study the effect of mesh size on the bearing dynamic coefficients. The mesh sizes used are 15×60, $30 \times 120, 45 \times 180$, and 90×360. In Figs. 6 and 7, the bearing dynamic coefficients are plotted versus misalignment angle θ_{x_0} at different mesh sizes. In Fig. 6, the plotted first-order coefficients are approximately identical for all coefficients except for K_{zz} and $K_{\theta_x\theta_x}$ over the full range of misalignment angle θ_{x_0}. The results of Fig. 7 show that the second-order bearing coefficients are approximately identical for all coefficients. However,

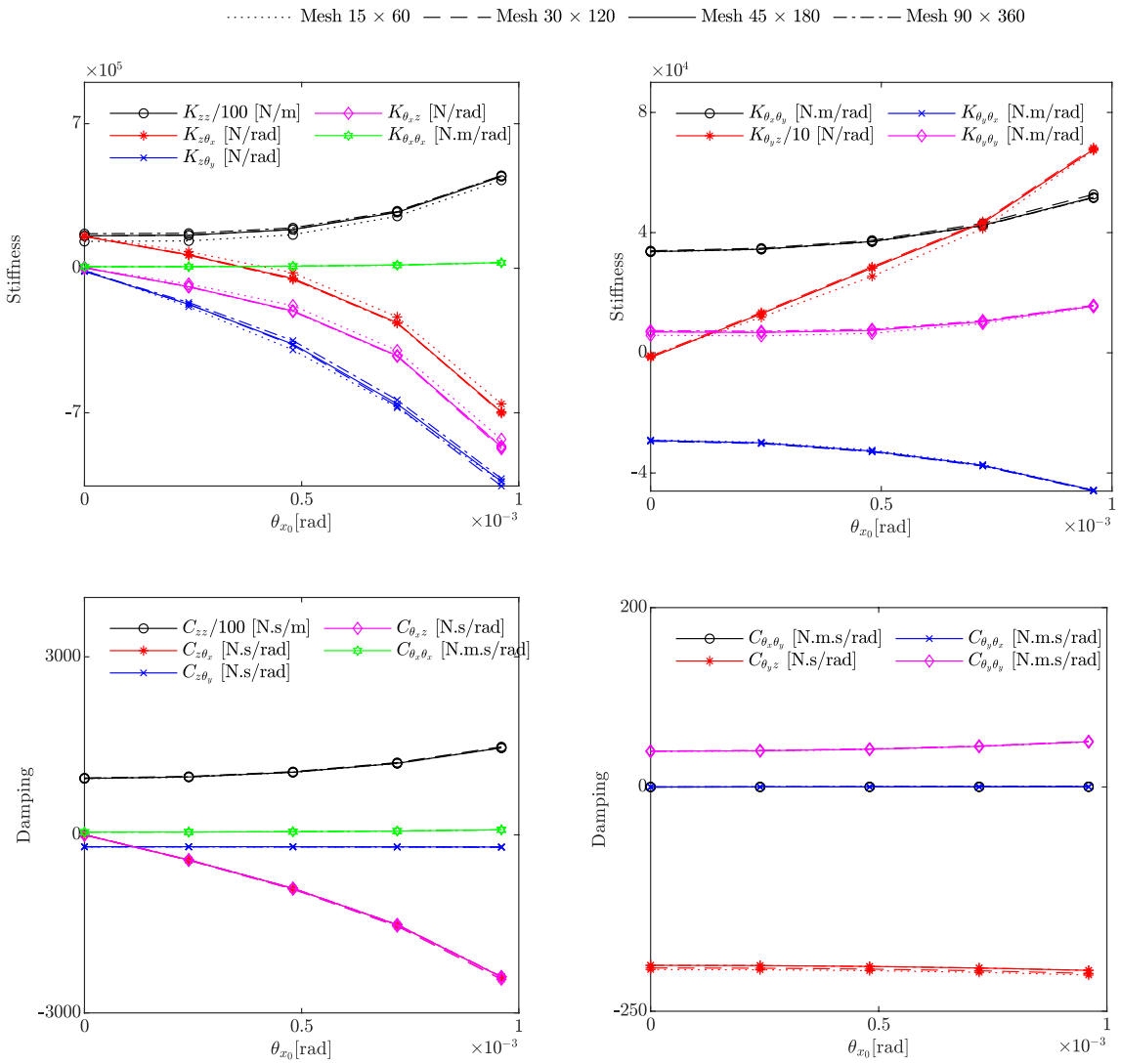

Fig. 6 Variation of first-order dynamic stiffness and damping coefficients with misalignment angle θ_{x_0} at different mesh sizes at $\theta_{x_0} \in [0, 0.96 \times 10^{-3}]$ radian, $n = 7200$ rpm, and $h_s = 10\,\mathrm{e}^{-6}$ m. In this figure, the dotted line for mesh 15×60, dashed line for mesh 30×120, solid line for mesh 45×180, and centerline for mesh 90×360

for $K_{zz\theta_x}, K_{z\theta_x\theta_x}, K_{\theta_y\theta_y\theta_y}, C_{\theta_y z\theta_x}$ and $C_{\theta_y z\theta_x}$ is mismatched. The mesh size 30×120 is used in calculating the bearing pressure and dynamic coefficient in the present paper. It is clear from the figure that, at a small perturbation, the direct stiffness and damping coefficients $(K_{zz}, C_{zz}, K_{\theta_x\theta_x}, K_{\theta_y\theta_y}, C_{\theta_x\theta_x}, C_{\theta_y\theta_y})$ increase with the increase of misalignment angle θ_{x_0}. In Fig. 7, the variation of the second-order stiffness and damping coefficients with misalignment angle θ_{x_0} is shown. As shown in the figure, most of the second-order coefficients tend to increase with the increase in the misalignment value, except for some coefficients such as $(K_{zzz}, K_{\theta_y zz}, K_{\theta_y z\theta_y}, K_{z\theta_x\theta_x}, K_{\theta_x z\theta_y}, C_{zzz}, C_{\theta_y z\theta_x}, C_{\theta_x z\theta_x})$ whose value decreases with the increase in the misalignment value. Also, the values of the damping coefficients $(C_{\theta_x zz}, C_{zz\theta_x})$ have the same values. The values of first- and second-order dynamic coefficients are illustrated in

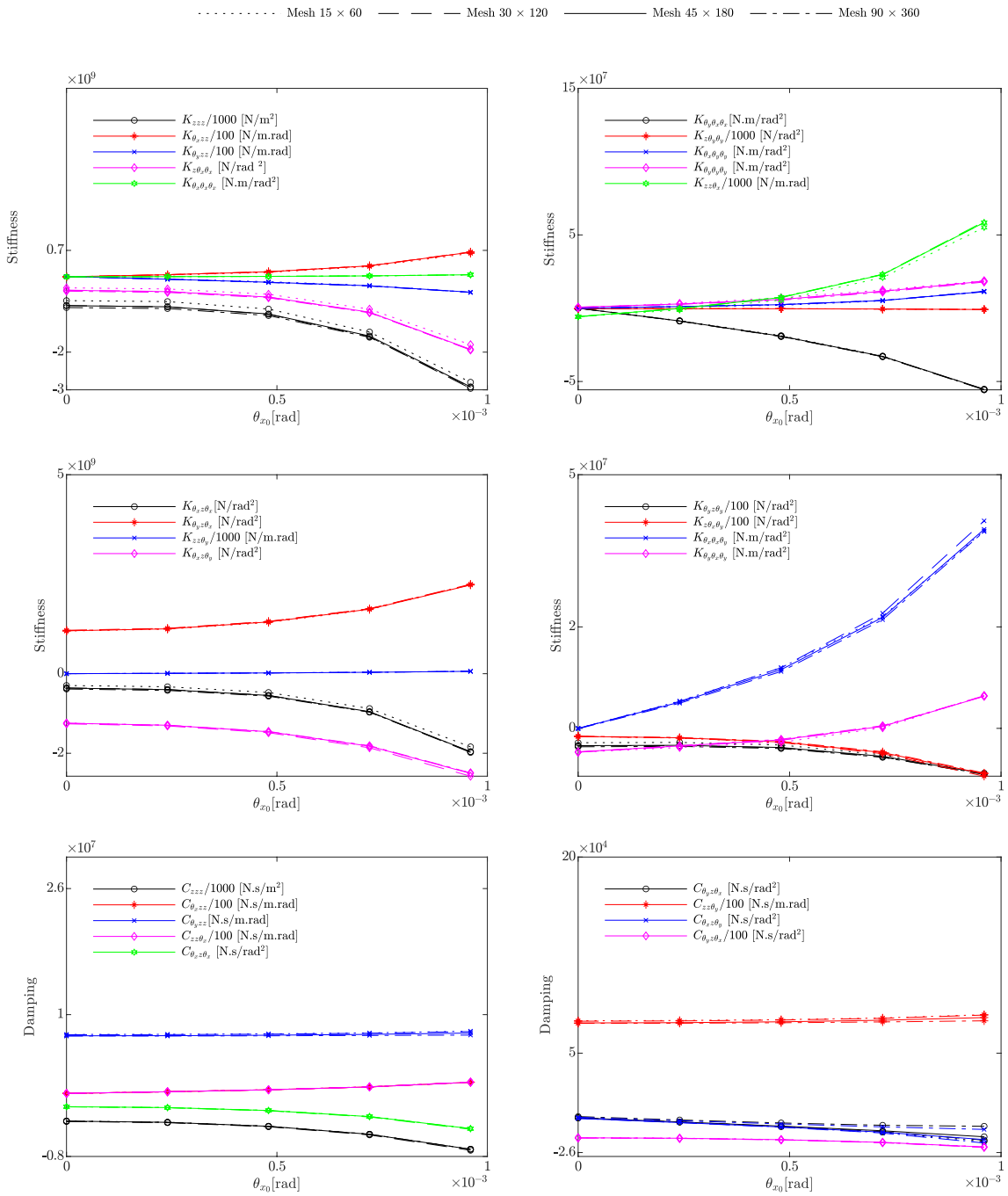

Fig. 7 Variation of second-order dynamic stiffness and damping coefficients with misalignment angle θ_{x_0} at different mesh sizes at $\theta_{x_0} \in [0, 0.96\,\text{e}{-3}]$ radian, $n = 7200$ rpm, and $h_s = 10\,\text{e}{-6}$ m. In this figure, the dotted line for mesh 15×60, dashed line for mesh 30×120, solid line for mesh 45×180, and centerline for mesh 90×360

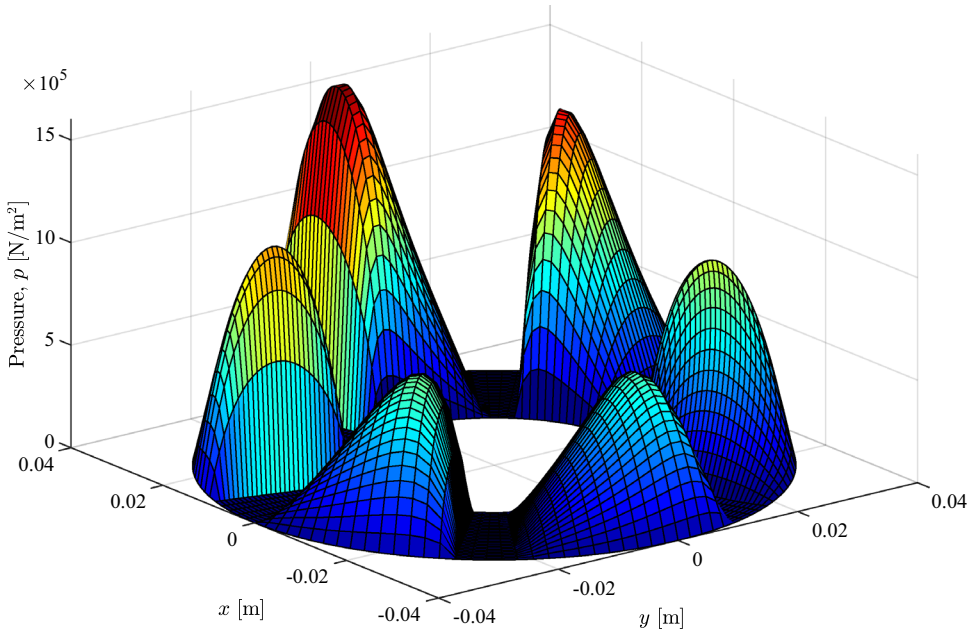

Fig. 8 Thrust bearing pressure distribution at $\theta_{x_0} = 0.48$ e−3 radian, $n = 7200$ rpm, and $h_s = 10$ e−6 m

Appendix A in Table 3 and 4, respectively, for mesh size of 30×120.

Effect of Inclined Film Thickness (h_s) on the Dynamic Coefficients

The dynamic coefficients of the inclined pad thrust bearing are investigated versus the variation of the inclined film thickness h_s of the thrust plate. The film thickness h_s assumed to change from 10×10^{-6} to 100×10^{-6} m at a rotational speed, n of 7200 rpm, and misalignment angle θ_{x_0} equal to 0.48 e−3 radian. The dynamic pressure distribution of the inclined pad thrust is shown in Fig. 8 with a film thickness $h_s = 10$ e−5. It is clear from Fig. 8 that the distribution of pressure has values on all parts of bearing pads unlike the previous state when changing the misalignment angle or subsequent state when changing the rotation speed, and the pressure has values in some of the bearing pads, while its value is equal to zero in the other pads. Figure 9 shows the variation of the first-order dynamic stiffness and damping coefficients with film thickness h_s. It is clear from the figure that the direct stiffness and damping coefficients (K_{zz}, C_{zz}) clearly have the greatest values among the rest of the coefficients. It is clear that the values of the stiffness and damping coefficients $(K_{z\theta_x}, K_{\theta_x z}, K_{z\theta_y}, K_{\theta_y z}, C_{zz}, C_{\theta_y\theta_y})$ decrease with increasing film thickness h_s. Also, the coupled damping coefficients $C_{\theta_y\theta_x}$ and $C_{\theta_x\theta_y}$ are equal. In Fig. 10, the variation of the second-order stiffness and damping coefficients with film thickness h_s is shown. As shown in the figure, most of the second-order coefficients tend to increase with the increase in the film thickness, except for some coefficients such as $(K_{\theta_y z\theta_x}, K_{\theta_x\theta_x\theta_y}, C_{zz\theta_x}, C_{zz\theta_y}, C_{\theta_x z\theta_y})$ whose value decreases with the increase in the film thickness value.

Effect of Rotational Speed (n) on the Dynamic Coefficients

To study the effect of rotational speed on the dynamic coefficient of the thrust bearing, a constant misalignment angle θ_{x_0} equal to 0.48×10^{-3} radian is considered, and the rotational speed varied from 2000 to 10,000 rpm. The dynamic pressure distribution of the inclined pad thrust is shown in Fig. 11 at a constant misalignment angle. The first-order stiffness and damping coefficients are shown in Fig. 12. It is noticeable from the figure that the stiffness coefficients change linearly with the rotational speed, while the damping coefficients remain constant as the rotational speed has no effect on it and $C_{\theta_x\theta_y} = C_{\theta_y\theta_x}$. Figure 13 shows the variations

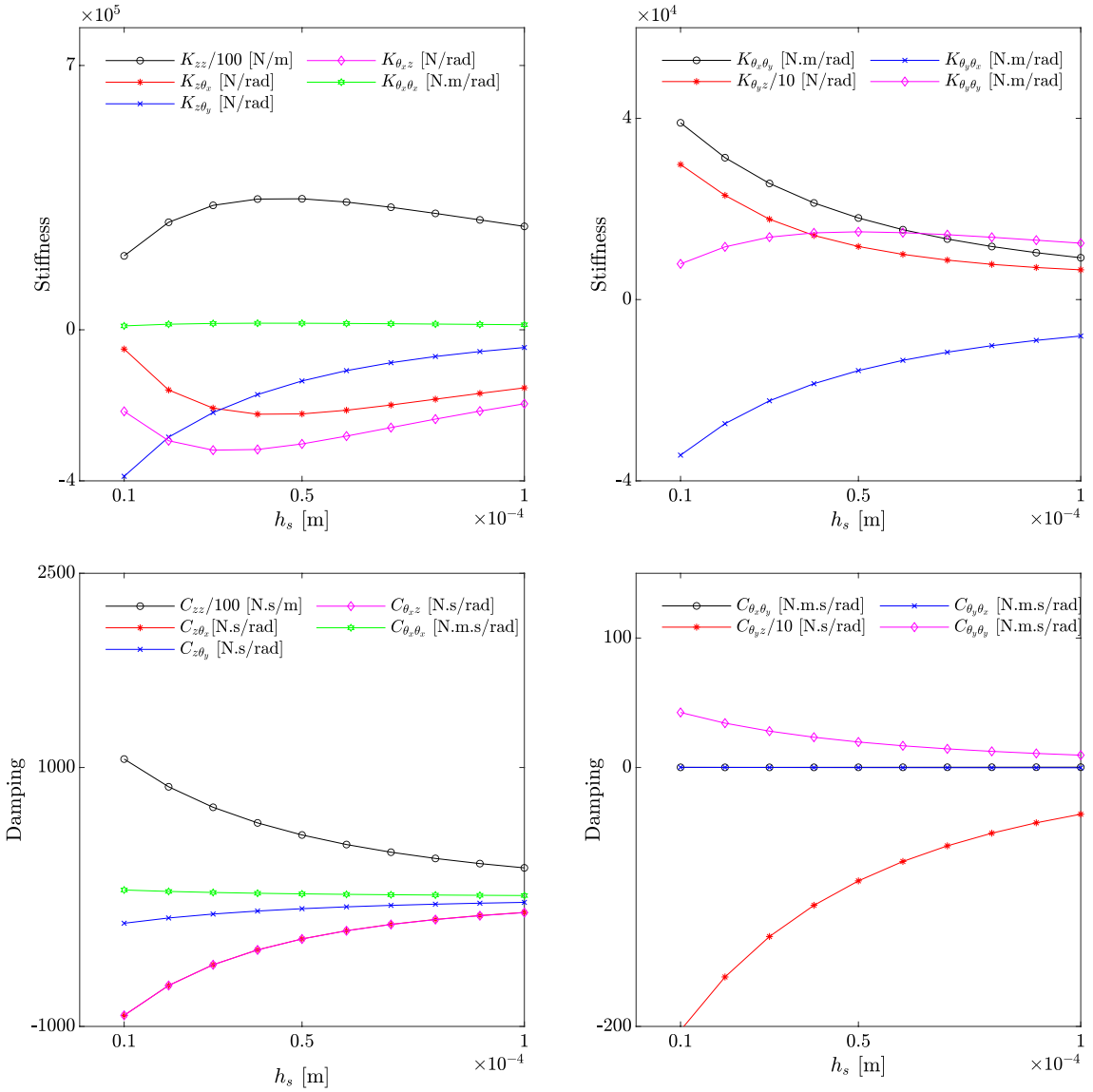

Fig. 9 Variation of first-order dynamic stiffness and damping coefficients with film thickness hs at $\theta_{x_0} = 0.48 \times 10^{-3}$ radian, $n = 7200$ rpm, and $h_s \in [1 - -10]\ \mathrm{e}^{-6}$ m

of the second-order dynamic stiffness and damping coefficients of the inclined pad thrust bearing versus rotational speed. From Fig. 13, it is clear that the rotational speed has no effect on the damping coefficients, while $C_{\theta_x zz} = C_{zz\theta_x}$. This is clear from Eqs. (8) and (14), as the rotational speed does not exist in the equations and therefore has no effect on the damping coefficients, whether of the first order or of the second order.

Conclusion

In this paper, the two-dimensional Reynolds equation is solved numerically to model the flow in the fluid film between the runner (collar) and the inclined pad thrust bearing. The effect of the shaft collar misalignment on the performance of hydrodynamic thrust bearing is investigated.

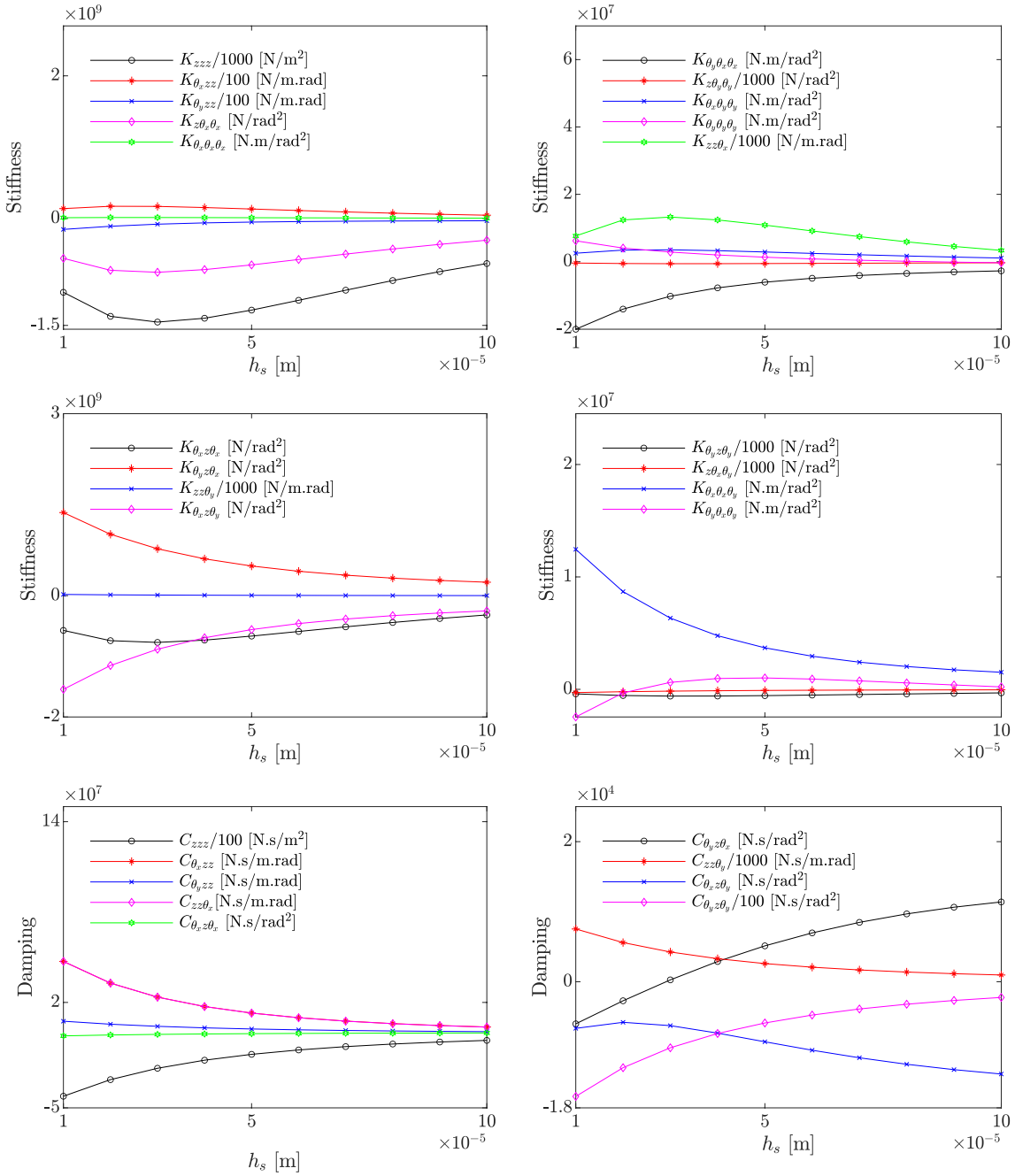

Fig. 10 Variation of second-order dynamic stiffness and damping coefficients with film thickness h_s at $\theta_{x_0} = 0.48$ e−3 radian, $n = 7200$ rpm, and $h_s \in [1 - -10]$ e−6 m

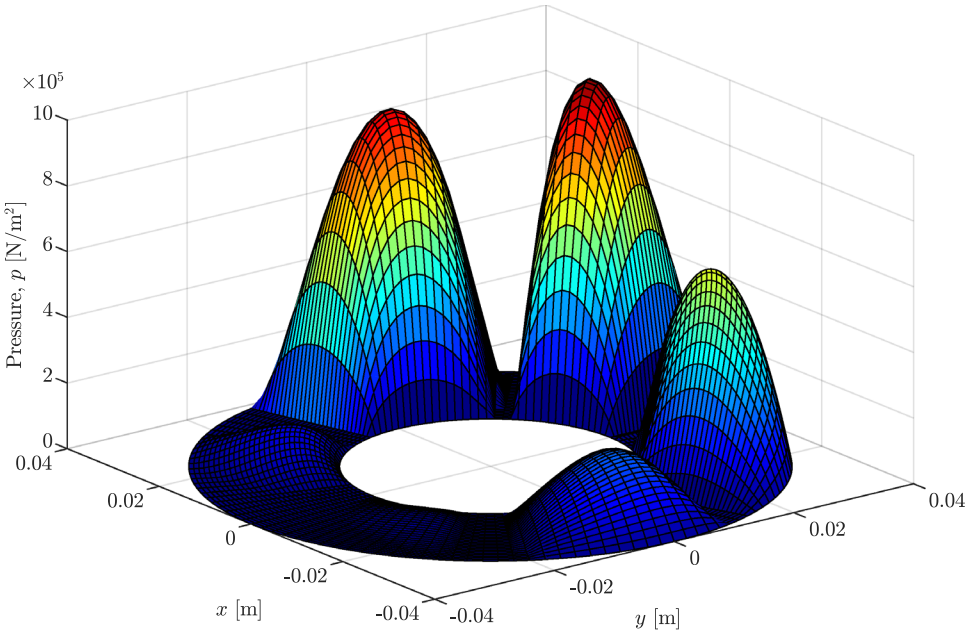

Fig. 11 Thrust bearing pressure distribution at $\theta_{x_0} = 0.48 \times 10^{-3}$ radian, $n = 10,000$ rpm, and $h_s = 10\text{e}{-5}$ m

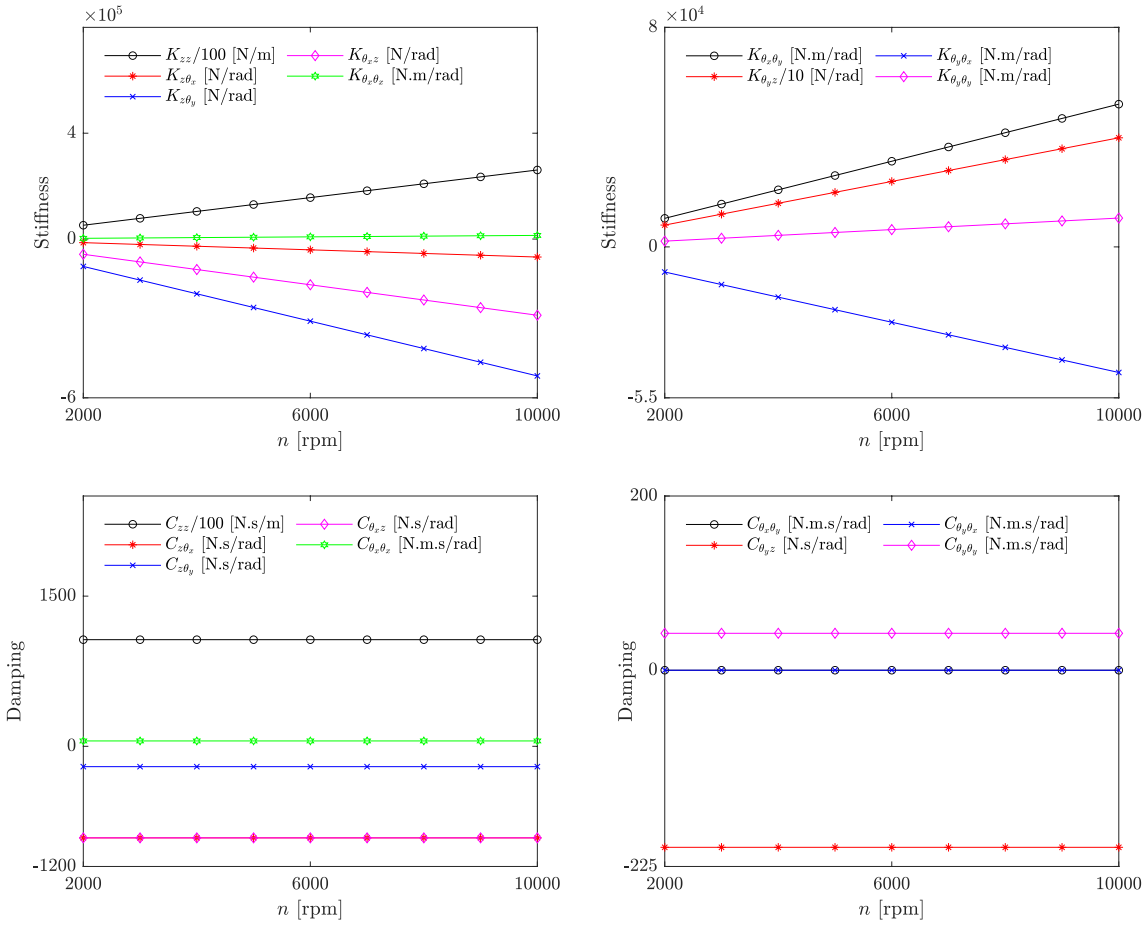

Fig. 12 Variation of first-order dynamic stiffness and damping coefficients with rotational speed n at $\theta_{x_0} = 0.48\ \text{e}^{-3}$ radian, $n \in [2000 - 10,000]$ rpm, and $h_s = 10\ \text{e}{-5}$ m

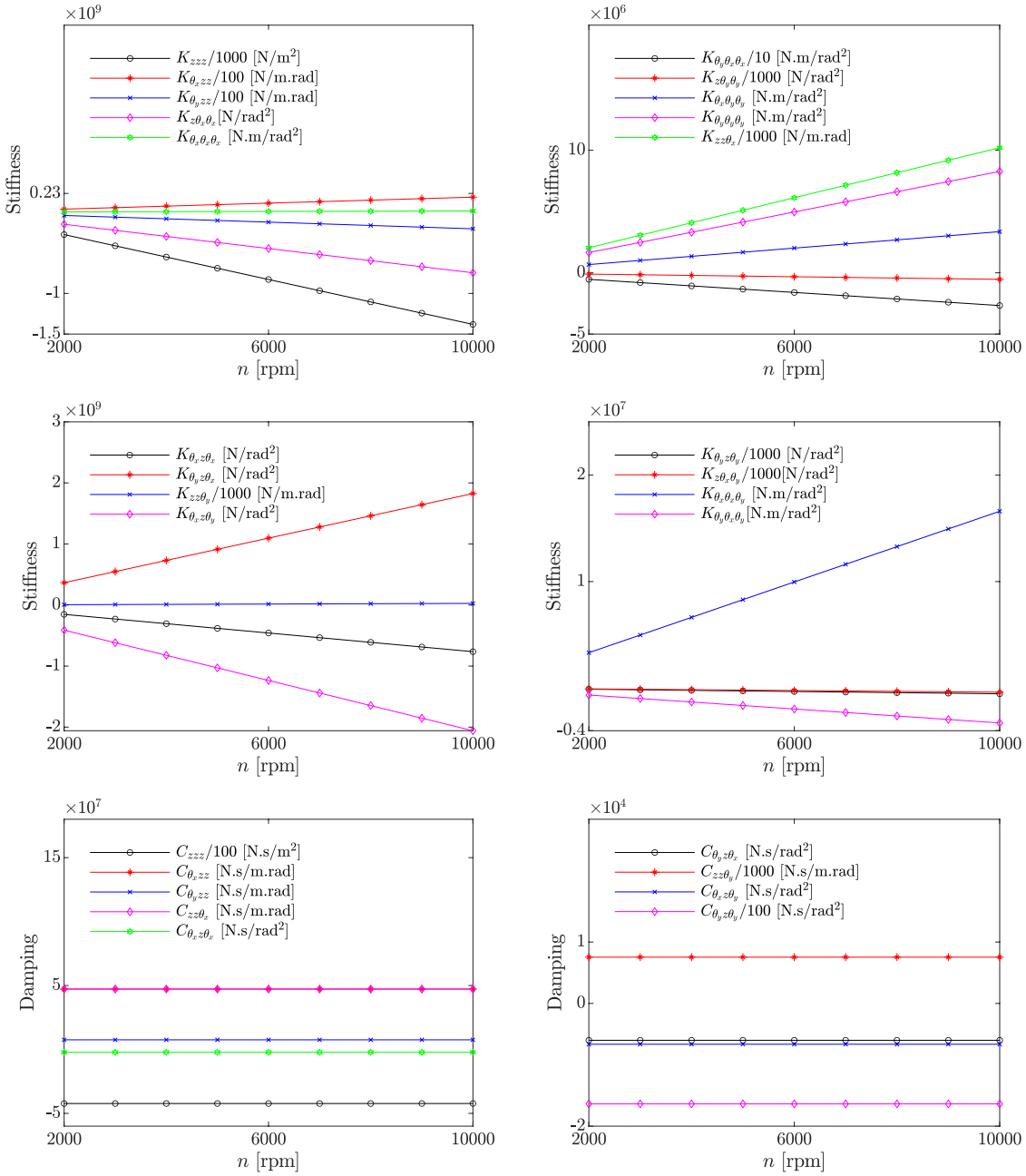

Fig. 13 Variation of second-order dynamic stiffness and damping coefficients with rotational speed n at $\theta_{x_0} = 0.48$ e−3 radian, $n \in [2000 - 10,000]$ rpm, and $h_s = 10$ e−5 m

The infinitesimal perturbation method is used to calculate the dynamic force and moment coefficients by applying a small misalignment in x-direction. The first-order dynamic coefficients as well as the second-order dynamic coefficients are evaluated. The effect of mesh size, misalignment, and rotational speed on the bearing dynamic coefficients are studied. Among the most important conclusions obtained from this paper are the following:

- The force and moment are calculated for the three different methods (based on Reynolds equation, the first-order coefficients, and the second-order coefficients) almost identical and this is an indication of the correctness of the calculation method used.
- The mesh size has a slight impact on some coefficients of the first- and second-order analysis.
- The dynamic coefficients change with misalignment in a non-linear way, while it changes with the rotational speed in a linear way.
- The effect of changing fluid film thickness on the mechanical coefficients of thrust bearing appears significantly, whether in the stiffness coefficients or the damping coefficients.
- The damping coefficients are not affected by the change in rotational speed.

The calculated dynamic coefficients in this paper may be used in further prediction of the dynamic characteristics of a rotor-bearing system.

Appendix A: The First- and Second-Order Dynamic Coefficients of the Thrust Bearing Used in the Calculations

See Tables 3 and 4.

Table 3 Second-order dynamic coefficients

θ_{x_0}	$K_{zz} \times 10^7$	$K_{z\theta_x} \times 10^5$	$K_{z\theta_y} \times 10^6$	$K_{\theta_x\theta_x} \times 10^4$	$K_{\theta_y\theta_y} \times 10^4$	$K_{\theta_x\theta_y} \times 10^4$	$K_{\theta_y\theta_x} \times 10^4$	$K_{\theta_x z} \times 10^5$	$K_{\theta_y z} \times 10^5$
0	1.5604	1.5539	−0.0111	0.7314	0.6981	3.3959	−2.9437	0.0169	−0.1144
0.00024	1.6004	0.6628	−0.1744	0.7862	0.6847	3.482	−3.0218	−0.8939	1.3425
0.00048	1.8793	−0.4893	−0.3724	0.9924	0.7562	3.7449	−3.2953	−2.0733	2.862
0.00072	2.7329	−2.6432	−0.6685	1.5374	1.0552	4.3067	−3.767	−4.2636	4.3647
0.00096	4.4901	−7.0252	−1.0545	2.7312	1.5807	5.2716	−4.6013	−8.7386	6.8248
θ_{x_0}	$C_{zz} \times 10^5$	$C_{z\theta_x} \times 10^3$	$C_{z\theta_y}$	$C_{\theta_x\theta_x}$	$C_{\theta_y\theta_y}$	$C_{\theta_x\theta_y}$	$C_{\theta_y\theta_x}$	$C_{\theta_x z} \times 10^3$	$C_{\theta_y z}$
0	0.9593	−0.0003	−201.7092	45.976	40.1512	−0.0041	−0.0104	−0.0002	−201.7286
0.00024	0.9845	−0.4283	−202.0487	47.8054	40.7178	0.0613	0.0548	−0.4283	−202.0161
0.00048	1.0651	−0.9144	−203.1379	53.7304	42.4899	0.1299	0.122	−0.9144	−203.033
0.00072	1.2187	−1.5373	−205.1051	65.2916	45.7186	0.2079	0.1965	−1.5373	−204.8684
0.00096	1.4848	−2.4323	−208.3807	86.0589	50.9245	0.3125	0.2925	−2.4323	−207.8438

Table 4 Second-order dynamic coefficients

θ_{x_0}	$K_{zzz}\times10^{12}$	$K_{\theta_x zz}\times10^{10}$	$K_{\theta_y zz}\times10^{10}$	$K_{zz\theta_x}\times10^{10}$	$K_{\theta_x z\theta_x}\times10^{9}$	$K_{\theta_y z\theta_x}\times10^{9}$	$K_{zz\theta_y}\times10^{10}$	$K_{\theta_x z\theta_y}\times10^{9}$	$K_{\theta_y z\theta_y}\times10^{9}$
0	−0.7645	−0.008	0.0539	−0.5789	−0.3612	1.0909	0.0528	−1.2599	−3.453
0.00024	−0.7991	0.5498	−0.6666	−0.0293	−0.4	1.1404	0.8746	−1.3132	−3.4176
0.00048	−0.9943	1.3266	−1.4759	0.7348	−0.5499	1.3149	1.9172	−1.4824	−3.8677
0.00072	−1.5917	2.9274	−2.4071	2.3148	−0.9661	1.6354	3.6076	−1.8611	−5.6681
0.00096	−2.9632	6.6043	−4.1302	5.9272	−1.9881	2.2499	6.1378	−2.5735	−9.1393
θ_{x_0}	$K_{z\theta_x\theta_x}\times10^{9}$	$K_{\theta_x\theta_x\theta_x}\times10^{7}$	$K_{\theta_y\theta_x\theta_x}\times10^{7}$	$K_{z\theta_x\theta_y}\times10^{8}$	$K_{\theta_x\theta_x\theta_y}\times10^{7}$	$K_{\theta_y\theta_x\theta_y}\times10^{6}$	$K_{z\theta_y\theta_y}\times10^{8}$	$K_{\theta_x\theta_y\theta_y}\times10^{7}$	$K_{\theta_y\theta_y\theta_y}\times10^{7}$
0	−0.3552	−0.0413	0.0022	−1.6056	−0.0004	−4.7038	−3.4098	−0.0071	0.045
0.00024	−0.3914	0.3777	−0.8784	−1.9	0.5314	−3.5542	−3.3915	0.114	0.2769
0.00048	−0.5373	1.0119	−1.9244	−2.7759	1.1954	−2.36	−3.8605	0.2417	0.5954
0.00072	−0.946	2.3359	−3.3073	−4.9975	2.2697	0.3825	−5.6886	0.5283	1.1586
0.00096	−1.943	5.4155	−5.5689	−9.4326	4.0906	6.4373	−9.1551	1.1558	1.8551
θ_{x_0}	$C_{zzz}\times10^{9}$	$C_{\theta_x zz}\times10^{8}$	$C_{\theta_y zz}\times10^{6}$	$C_{zz\theta_x}\times10^{8}$	$C_{\theta_x z\theta_x}\times10^{6}$	$C_{\theta_y z\theta_x}\times10^{4}$	$C_{zz\theta_y}\times10^{6}$	$C_{\theta_x z\theta_y}\times10^{4}$	$C_{\theta_y z\theta_y}\times10^{6}$
0	−3.5567	0.0001	7.4456	0.0001	−1.7046	−0.0548	7.4447	0.009	−1.4897
0.00024	−3.7133	0.214	7.463	0.214	−1.8186	−0.2649	7.4667	−0.3139	−1.5249
0.00048	−4.228	0.4723	7.5251	0.4723	−2.1994	−0.6007	7.5358	−0.665	−1.6369
0.00072	−5.2632	0.8407	7.6414	0.8407	−2.9904	−1.0047	7.6665	−1.1095	−1.8484
0.00096	−7.216	1.4495	7.852	1.4495	−4.5559	1.6521	7.9149	−1.8685	−2.2095
θ_{x_0}	$K_{zzz}\times10^{12}$	$K_{\theta_x zz}\times10^{10}$	$K_{\theta_y zz}\times10^{10}$	$K_{zz\theta_x\times10^{10}}$	$K_{\theta_x z\theta_x}\times10^{9}$	$K_{\theta_y z\theta_x}\times10^{9}$	$K_{zz\theta_y}\times10^{10}$	$K_{\theta_x z\theta_y}\times10^{9}$	$K_{\theta_y z\theta_y}\times10^{9}$
0	−0.7645	−0.008	0.0539	−0.5789	−0.3612	1.0909	0.0528	−1.2599	−3.453
0.00024	−0.7991	0.5498	−0.6666	−0.0293	−0.4	1.1404	0.8746	−1.3132	−3.4176
0.00048	−0.9943	1.3266	−1.4759	0.7348	−0.5499	1.3149	1.9172	−1.4824	−3.8677
0.00072	−1.5917	2.9274	−2.4071	2.3148	−0.9661	1.6354	3.6076	−1.8611	−5.6681
0.00096	−2.9632	6.6043	−4.1302	5.9272	−1.9881	2.2499	6.1378	−2.5735	−9.1393
θ_{x_0}	$K_{z\theta_x\theta_x}\times10^{9}$	$K_{\theta_x\theta_x\theta_x}\times10^{7}$	$K_{\theta_y\theta_x\theta_x}\times10^{7}$	$K_{z\theta_x\theta_y}\times10^{8}$	$K_{\theta_x\theta_x\theta_y}\times10^{7}$	$K_{\theta_y\theta_x\theta_y}\times10^{6}$	$K_{z\theta_y\theta_y}\times10^{8}$	$K_{\theta_x\theta_y\theta_y}\times10^{7}$	$K_{\theta_y\theta_y\theta_y}\times10^{7}$
0	−0.3552	−0.0413	0.0022	−1.6056	−0.0004	−4.7038	−3.4098	−0.0071	0.045
0.00024	−0.3914	0.3777	−0.8784	−1.9	0.5314	−3.5542	−3.3915	0.114	0.2769
0.00048	−0.5373	1.0119	−1.9244	−2.7759	1.1954	−2.36	−3.8605	0.2417	0.5954
0.00072	−0.946	2.3359	−3.3073	−4.9975	2.2697	0.3825	−5.6886	0.5283	1.1586
0.00096	−1.943	5.4155	−5.5689	−9.4326	4.0906	6.4373	−9.1551	1.1558	1.8551
θ_{x_0}	$C_{zzz}\times10^{9}$	$C_{\theta_x zz}\times10^{8}$	$C_{\theta_y zz}\times10^{6}$	$C_{zz\theta_x}\times10^{8}$	$C_{\theta_x z\theta_x}\times10^{6}$	$C_{\theta_y z\theta_x}\times10^{4}$	$C_{zz\theta_y}\times10^{6}$	$C_{\theta_x z\theta_y}\times10^{4}$	$C_{\theta_y z\theta_y}\times10^{6}$
0	−3.5567	0.0001	7.4456	0.0001	−1.7046	−0.0548	7.4447	0.009	−1.4897
0.00024	−3.7133	0.214	7.463	0.214	−1.8186	−0.2649	7.4667	−0.3139	−1.5249
0.00048	−4.228	0.4723	7.5251	0.4723	−2.1994	−0.6007	7.5358	−0.665	−1.6369
0.00072	−5.2632	0.8407	7.6414	0.8407	−2.9904	−1.0047	7.6665	−1.1095	−1.8484
0.00096	−7.216	1.4495	7.852	1.4495	−4.5559	1.6521	7.9149	−1.8685	−2.2095

Appendix B: Numerical Analysis Flowchart

In this Appendix, a flowchart for the numerical analysis used to obtain the paper results is presented (Fig. 14).

Author Contributions All authors contributed to the study conception and design. Material preparation, data collection, and analysis were performed by SK and HS. The first draft of the manuscript was written by SK and all authors commented on previous versions of the manuscript. All authors read and approved the final manuscript.

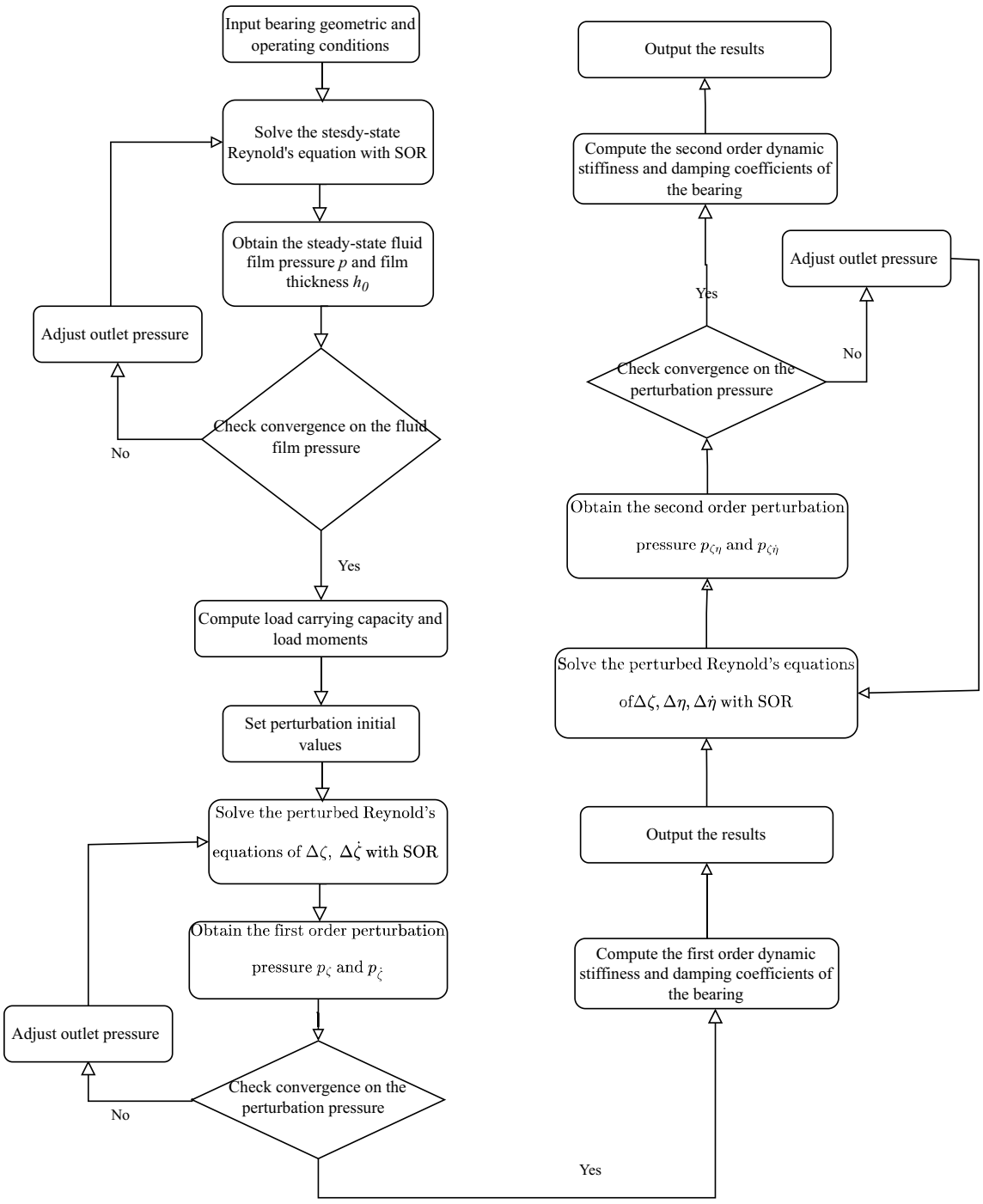

Fig. 14 Flowchart for the numerical analysis

Funding The authors declare that no funds, grants, or other supports were received during the preparation of this manuscript.

Data availability The datasets generated during and/or analyzed during the current study are available from the corresponding author on reasonable request.

Declarations

Conflict of Interest The authors have no relevant financial or non-financial interests to disclose.

References

1. Dimond T, Younan A, Allaire P (2011) A review of tilting pad bearing theory. Int J Rotat Mach. https://doi.org/10.1155/2011/908469
2. Reynolds O (1886) IV. On the theory of lubrication and its application to Mr. Beauchamp tower's experiments, including an experimental determination of the viscosity of olive oil. Philos Trans R Soc Lond 177:157–234
3. Pinkus O, Lynn W (1958) Solution of the tapered-land sector thrust bearing. Trans ASME 80(7):1510–1516
4. Najar FA, Harmain G (2014) Numerical investigation of pressure profile in hydrodynamic lubrication thrust bearing. Int Schl Res Not. https://doi.org/10.1155/2014/157615
5. Koç E (1990) An investigation into the numerical solution of Reynolds' lubrication equation with special reference to thrust bearings. Tribol Int 23(6):429–437
6. Heshmat H, Pinkus O (1987) Misalignment in thrust bearings including thermal and cavitation effects. J Tribol 109:108–114
7. Someya T, Fukuda M (1972) Analysis and experimental verification of dynamic characteristics of oil film thrust bearings. Bull JSME 15(86):1004–1015
8. Vieira L, Cavalca K, Nomura P (2011) Analysis of stiffness and damping coefficients of lubricated thrust bearings. In: Vibration Problems ICOVP 340
9. Vieira LC, Cavalca KL, Nomura PO (2010) Hydrodynamic lubrication evaluation of thrust bearings. In: SAE Technical Paper Series
10. Ettles C (1976) The development of a generalized computer analysis for sector shaped tilting pad thrust bearings. ASLE Trans 19(2):153–163
11. Zhang H, Zheng W, Li F (2020) Simulation design and numerical analysis of bearing capacity of water lubricated thrust bearing. IOP Conf Ser 446(5):6
12. Najar FA, Harmain G (2016) Performance characteristics in hydrodynamic water cooled thrust bearings. J Tribol 10:28–47
13. Kim H, Jang G, Ha H (2012) A generalized Reynolds equation and its perturbation equations for fluid dynamic bearings with curved surfaces. Tribol Int 50:6–15
14. Liming Z, Yongyao L, Zhengwei W, Xin L, Yexiang X (2017) A review on the large tilting pad thrust bearings in the hydropower units. Renew Sustain Energy Rev 69:1182–1198
15. Jang G, Lee S (2006) Determination of the dynamic coefficients of the coupled journal and thrust bearings by the perturbation method. Int Jt Tribol Conf 42592:445–453
16. Lin X, Wang R, Zhang S, Jiang S (2020) Study on dynamic characteristics for high speed water-lubricated spiral groove thrust bearing considering cavitating effect. Tribol Int 143:106022
17. Zhang S, Jiang S, Lin X (2020) Static and dynamic characteristics of high-speed water-lubricated spiral-groove thrust bearing considering cavitating and centrifugal effects. Tribol Int 145:106159
18. Lin X, Wang S, Jiang S, Zhang S (2022) Dynamic characteristics of high-speed water-lubricated spiral groove thrust bearing based on turbulent cavitating flow lubrication model. Chin J Mech Eng 35(1):1–21
19. Jialei D, Liang G (2020) Dynamic coefficients and stability analysis of a water-lubricated hydrostatic bearing by solving the uncoupled Reynolds equation. Chin J Aeronaut 33(8):2110–2122
20. Peixoto TF, Daniel GB, Cavalca KL (2017) Experimental estimation of equivalent damping coefficient of thrust bearings. International symposium on dynamic problems of mechanics. Springer, Cham, pp 17–29
21. Peixoto TF, Daniel GB, Cavalca KL (2018) Thermo-hydrodynamic model influence on first order coefficients in turbocharger thrust bearings. International conference on rotor dynamics. Springer, Cham, pp 16–31
22. Peixoto TF, Cavalca KL (2019) Investigation on the angular displacements influence and nonlinear effects on thrust bearing dynamics. Tribol Int 131:554–566
23. Peixoto TF, Cavalca KL (2020) Thrust bearing coupling effects on the lateral dynamics of turbochargers. Tribol Int 145:106166
24. Yadav SK, Rajput AK, Ram N, Sharma SC (2018) A novel technique to compute static and dynamic performance characteristics of aerostatic thrust bearing. Ind Lubric Tribol. https://doi.org/10.1108/ILT-04-2017-0090
25. Lin J-R, Hung C-R (2004) Analysis of dynamic characteristics for wide slider bearings with an exponential film profile. J Mar Sci Technol 12(3):217–221
26. Koutsoumpas G, Charitopoulos A, Papadopoulos CI, Fillon M (2020) Computational evaluation of dynamic coefficients of thrust bearings: effect of artificial texturing on thermohydrodynamic performance. Surf Topogr Metrol Prop 8(2):024009
27. Srikanth D, Chaturvedi KK, Reddy ACK (2012) Determination of a large tilting pad thrust bearing angular stiffness. Tribol Int 47:69–76
28. Iordanoff I, Stefan P, Boudet R, Poirier D (1995) Dynamic analysis of a thrust bearing-effect of misalignment and load. Proc Inst Mech Eng Part J 209(3):189–194
29. Jiang P, Yu L (1999) Dynamics of a rotor-bearing system equipped with a hydrodynamic thrust bearing. J Sound Vib 227(4):833–872
30. Storteig E, White MF (1999) Dynamic characteristics of hydrodynamically lubricated fixed-pad thrust bearings. Wear 232(2):250–255
31. Gad AM (2016) Effect of misalignment on the durability of gas-lubricated foil thrust bearing. J Eng Sci 44(1):73–90
32. Gad AM (2017) On the performance of foil thrust bearing with misaligned bearing runner. Ind Lubric Tribol 69(2):105–115
33. Shi J, Cao H, Jin X (2019) Investigation on the static and dynamic characteristics of 3-DOF aerostatic thrust bearings with orifice restrictor. Tribol Int 138:435–449
34. San-Andre's L (2002) Effects of misalignment on turbulent flow hybrid thrust bearings. J Tribol 124(1):212–219

35. Sun F, Zhang X, Wei Y, Wang X, Wang D (2020) Stability analysis of rubber-supported thrust bearing in a rotor-bearing system used in marine thrusters under disturbing moments. Tribol Int 151:106356
36. Nitzschke S, Ziese C, Woschke E (2021) Analysis of dynamical behaviour of full-floating disk thrust bearings. Technical sciences. Bull Pol Acad Sci 69:e139001–e139001
37. Jang G, Kim Y (1999) Calculation of dynamic coefficients in a hydrodynamic bearing considering five degrees of freedom for a general rotor-bearing system. J Tribol. https://doi.org/10.1115/1.2834095
38. Jintanawan T, Ku C-PR, Zhu J (2004) Effects of thrust hydrodynamic bearing stiffness and damping on disk-spindle axial vibration in hard disk drives. Microsyst Technol 10(4):338–344
39. Temis M, Lazarev A (2012) Elastohydrodynamic contact model for calculation of axial and angular stiffness in thrust bearing. Arch Mech Eng 59(4):453
40. Srikanth D, Chaturvedi K, Reddy A (2009) Modelling of large tilting pad thrust bearing stiffness and damping coefficients. Tribol Ind 31(3 &4):23–27
41. Miraskari M, Hemmati F, Gadala MS (2018) Nonlinear dynamics of flexible rotors supported on journal bearings-part i: analytical bearing model. J Tribol. https://doi.org/10.1115/1.4037730
42. Miraskari M, Hemmati F, Gadala MS (2018) Nonlinear dynamics of flexible rotors supported on journal bearings-part ii: numerical bearing model. J Tribol 140(2):021705. https://doi.org/10.1115/1.4037731
43. Weimin W, Lihua Y, Tiejun W, Lie Y (2012) Nonlinear dynamic coefficients prediction of journal bearings using partial derivative method. Proc Inst Mech Eng Part J 226(4):328–339. https://doi.org/10.1177/1350650111431526
44. Sayed H, El-Sayed TA (2022) Nonlinear dynamics and bifurcation analysis of journal bearings based on second order stiffness and damping coefficients. Int J Non-Linear Mech 142:103972. https://doi.org/10.1016/j.ijnonlinmec.2022.103972
45. Sayed H, El-Sayed TA (2022) A novel method to evaluate the journal bearing forces with application to flexible rotor model. Tribol Int 173:107593. https://doi.org/10.1016/j.triboint.2022.107593
46. El-Sayed TA, Sayed H (2022) Bifurcation analysis of rotor/bearing system using third-order journal bearing stiffness and damping coefficients. Nonlinear Dyn 107(1):123–151. https://doi.org/10.1007/s11071-021-06965-4
47. Meruane V, Pascual R (2008) Identification of nonlinear dynamic coefficients in plain journal bearings. Tribol Int 41(8):743–754. https://doi.org/10.1016/j.triboint.2008.01.002